The Meteoritical Society

Meteoritics & Planetary Science 50, Nr 12, 2024–2044 (2015)
doi: 10.1111/maps.12571

Petrography and geochemistry of the enriched basaltic shergottite Northwest Africa 2975

Qi HE[1*], Long XIAO[1], J. Brian BALTA[2], Ioannis P. BAZIOTIS[3], Weibiao HSU[4], and Yunbin GUAN[5]

[1]Planetary Science Institute, School of Earth Sciences, China University of Geosciences, Wuhan 430074, China
[2]Department of Geology and Planetary Sciences, University of Pittsburgh, Pittsburgh, Pennsylvania 15217, USA
[3]Agricultural University of Athens, Laboratory of Mineralogy and Geology, Athens 11855, Greece
[4]Laboratory for Astrochemistry and Planetary Sciences, Purple Mountain Observatory, Chinese Academy of Sciences, Nanjing 210008, China
[5]Division of Geological and Planetary Sciences, California Institute of Technology, Pasadena, California 91125, USA
[*]Corresponding author. E-mail: qihe_cug@yahoo.com

(Received 30 July 2013; revision accepted 30 September 2015)

Abstract–We present a study of the petrology and geochemistry of basaltic shergottite Northwest Africa 2975 (NWA 2975). NWA 2975 is a medium-grained basalt with subophitic to granular texture. Electron microprobe (EMP) analyses show two distinct pyroxene compositional trends and patchy compositional zoning patterns distinct from those observed in other meteorites such as Shergotty or QUE 94201. As no bulk sample was available to us for whole rock measurements, we characterized the fusion crust and its variability by secondary ion mass spectrometer (SIMS) measurements and laser ablation inductively coupled plasma spectroscopy (LA-ICP-MS) analyses as a best-available proxy for the bulk rock composition. The fusion crust major element composition is comparable to the bulk composition of other enriched basaltic shergottites, placing NWA 2975 within that sample group. The CI-normalized REE (rare earth element) patterns are flat and also parallel to those of other enriched basaltic shergottites. Merrillite is the major REE carrier and has a flat REE pattern with slight depletion of Eu, parallel to REE patterns of merrillites from other basaltic shergottites. The oxidation state of NWA 2975 calculated from Fe-Ti oxide pairs is NNO-1.86, close to the QFM buffer. NWA 2975 represents a sample from the oxidized and enriched shergottite group, and our measurements and constraints on its origin are consistent with the hypothesis of two distinct Martian mantle reservoirs: a reduced, LREE-depleted reservoir and an oxidized, LREE-enriched reservoir. Stishovite, possibly seifertite, and dense SiO_2 glass were also identified in the meteorite, allowing us to infer that NWA 2975 experienced a realistic shock pressure of ~30 GPa.

INTRODUCTION

In the absence of returned samples, Martian meteorites provide the only opportunity to directly study Martian magmatic and planetary differentiation processes. The rarer groups of Martian meteorites are older than 1 Ga and include cumulate rocks such as the nakhlites, two chassignites, ALH 84001, and the newly discovered crustal meteorite NWA 7034 (Brandon et al. 2000; Treiman 2005; Lapen et al. 2010; Agee et al. 2013). The majority of the Martian meteorites, the shergottites, are basaltic in composition and have ages younger than 500 Ma, demonstrating that Mars was still volcanically active as recently as 170 Ma ago (Nyquist et al. 2001; Herd et al. 2007; Misawa and Yamaguchi 2007; Niihara 2011; Zhou et al. 2013; Moser et al. 2013). Shergottites consequently provide information about both Martian differentiation and the nature of recent Martian magmatism. Petrographically they are classified into three subgroups: basaltic, olivine-phyric, and lherzolitic (Goodrich 2002), while based on their rare earth element (REE) and isotopic compositions they are classified as enriched (Shergotty, Zagami, etc.), intermediate (ALHA77005), and depleted

(SaU 005, QUE 94201, Tissint) (Bridges and Warren 2006; Symes et al. 2008; Papike et al. 2009; Balta et al. 2015). Shergottites also cover a wide range in fO_2 from QFM-4 to QFM (Wadhwa 2001; Herd 2003; Goodrich 2003; Symes et al. 2008; Papike et al. 2009; Balta et al. 2015) with oxygen fugacities correlated with REE abundances and isotopic compositions. However, whether the geochemical variations observed in shergottites result from crustal contamination during magma ascent (e.g., Wadhwa 2001; Herd et al. 2002) or from melting of distinct mantle reservoirs (e.g., Borg and Draper 2003; Debaille et al. 2008; Hui et al. 2011) remains a controversy.

NWA 2975 is a basaltic shergottite found in Morocco in 2005 (see Meyer 2012). Preliminary study of its petrology and mineralogy indicated that it is one of the more evolved basaltic shergottites, similar to Shergotty and Los Angeles (Wittke et al. 2006). However, studies on NWA 2975 are currently limited, with only several abstracts presented (e.g., Wittke et al. 2006; Sanborn and Wadhwa 2010; He et al. 2011; Lindsay et al. 2013). To better characterize the petrogenesis of NWA 2975, we carried out detailed petrological, mineralogical, and geochemical studies on a section of this meteorite. In addition, we report characterization of shock metamorphism features in our NWA 2975 section, with emphasis on estimating minimum shock pressures. Our goals are to constrain the petrogenetic history of NWA 2975, clarify its relationship with the other known shergottites, establish its redox state, and provide new insights into Martian magmatic history.

ANALYTICAL METHODS

We characterized the mineralogy, texture, and petrography of NWA 2975 on a polished thick section (6 fragments of 2–3 mm across) embedded in epoxy resin. Backscattered electron (BSE) imaging and X-ray mapping were carried out using a scanning electron microscope (SEM, JEOL-845) with an energy dispersive spectrometer (EDS) at Purple Mountain Observatory, Nanjing. A field emission scanning electron microscope (FE-SEM, FEI Quanta 450) at the State Key Laboratory of Geological Processes and Mineral Resources, China University of Geosciences, Wuhan, was also used to obtain BSE images at higher magnification.

We analyzed mineral compositions with an EMP (JEOL 8100 at China University of Geosciences, Wuhan). Accelerating voltage was set at 15 keV and beam current was set at 20 nA with a focused beam of 1 μm for most silicate and oxide minerals. Peak and background counting times for most elements were 10 s and 5 s, respectively. Both synthetic (NBS) and natural mineral standards (such as plagioclase, diopside, andradite, rutile, apatite, and so on) were used. Matrix corrections were based on ZAF procedures. Typical detection limits for oxides of most elements are 0.03 wt%. The phosphates and glassy phases (including the plagioclase glass and the fusion crust) were analyzed at 10 nA beam current with a defocused beam diameter of 5–10 μm. Mikouchi et al. (1999) reported Na loss from plagioclase glass under electron beam; however, our analyses on maskelynite using defocused beams do not show significant Na loss.

We collected Raman spectra of plagioclase, baddeleyite, and other minerals using a Thermo Scientific DXR dispersive Raman micro-spectrometer at the State Key Laboratory of Geological Processes and Mineral Resources, China University of Geosciences, Wuhan. It is equipped with a 532 nm Nd-YVO4 laser, ×100 objective lens and an automated confocal microscope (Olympus BX51). The laser beam with an output power of 24 mW irradiated the sample with a maximum power of 10 mW and an estimated spot size of 1 μm; such laser power is low enough to avoid destruction of the irradiated area. Raman spectra were collected in 10 accumulations of 5 s each. Peak identification was done with the Thermo Scientific OMNIC™ software. The frequencies of the Raman bands were monitored by the 1001 cm^{-1} band of the standard polystyrene before and after each measurement, and the band-frequency accuracy was about 0.5 cm^{-1} (1σ level). Standard spectra were obtained from an internal Raman database provided by the RRUFF project (Handbook of Raman Spectra; Downs 2006; and http://rruff.info/) and published data. Each Raman spot has been coupled with an EMP analysis for a complete mineral identification (chemistry and structure).

We measured abundances of REE and other trace elements in situ on mineral grains of pyroxene, plagioclase, merrillite, and fusion crust glasses with SIMS (secondary ion mass spectrometer, the Cameca 7f-Geo ion microprobe of the California Institute of Technology, USA). A −13.5 Kev, 1–4 nA O^- primary ion beam of about 20 μm in diameter was used to sputter the sample. Secondary ions, energy filtered by −80 eV from a nominal +9 keV, were collected in peak-jumping mode with an electron multiplier. The energy bandwidth was set at 45 eV. Silicon and calcium were used as reference elements for silicates and phosphates, respectively. Concentrations of reference elements (SiO_2 and CaO) were derived from EMP measurements on the specific grains chosen for ion probe analysis. The NBS-610 and NBS-612 glass standards were measured periodically to account for any variation in ionization

efficiencies caused by minor changes of operating conditions. The analytical errors reported are 1σ and are based on counting statistics only.

Major and trace element analyses of fusion crust and melt pocket glasses were conducted by laser ablation inductively coupled plasma mass spectrometry (LA-ICP-MS) at the State Key Laboratory of Geological Processes and Mineral Resources, China University of Geosciences, Wuhan. Detailed operating conditions for the laser ablation system and the ICP-MS instrument and data reduction are as described by Liu et al. (2008). Laser sampling was performed using a GeoLas 2005 (an excimer 193 nm laser ablation system). An Agilent 7500a ICP-MS instrument was used to acquire ion-signal intensities. Helium was applied as a carrier gas. Argon was used as the make-up gas and mixed with the carrier gas via a T-connector before entering the ICP. Nitrogen was added into the central gas flow (Ar + He) of the Ar plasma to decrease the detection limit and improve precision (Hu et al. 2008). Each analysis incorporated a background acquisition of approximately 20–30 s (gas blank) followed by a 50 s data acquisition from the sample. The Agilent Chemstation was utilized for the acquisition of each individual analysis. Element contents were calibrated against multiple-reference materials (BCR-2G and BHVO-2G) without applying internal standardization (Liu et al. 2008). Off-line selection and integration of background and analyte signals and time-drift correction and quantitative calibration for trace element analyses were performed by ICPMSDataCal (Liu et al. 2008, 2010). All data were acquired at a spot size of 44 μm.

PETROGRAPHY AND MINERAL CHEMISTRY

NWA 2975 is a basaltic shergottite and is possibly paired with NWA 2986 (see Meyer [2012] for description). It is a medium-grained, subophitic- to granular-textured basalt composed primarily of clinopyroxene and maskelynite (up to ~2 mm in the largest dimension), with some preferred orientation of prismatic clinopyroxene grains (Fig. 1A, see also fig. 3 in Wittke et al. 2006). Fresh fusion crusts (partial) are observed in our section (Fig. 1B). Shock-induced melt veins (about 20-40 μm in width) and pockets (mostly 1–3 mm) are abundant (Figs. 1B and 1C). Wittke et al. (2006) reported melt pockets up to 6 mm across and glass veins up to 3 mm wide, but that was in reference to the hand-specimen samples. The observed shock melt pockets are usually round or irregular shaped and occur adjacent to pyroxene and maskelynite. Our fragments of NWA 2975 have significant fusion crust glass on their perimeters. The fusion crust varies in thickness from approximately 0.03 to 0.3 mm and abundant vesicles are found within it. Heterogeneity of fusion crust composition can be seen as different shades of gray to white in BSE images (Fig. 1B).

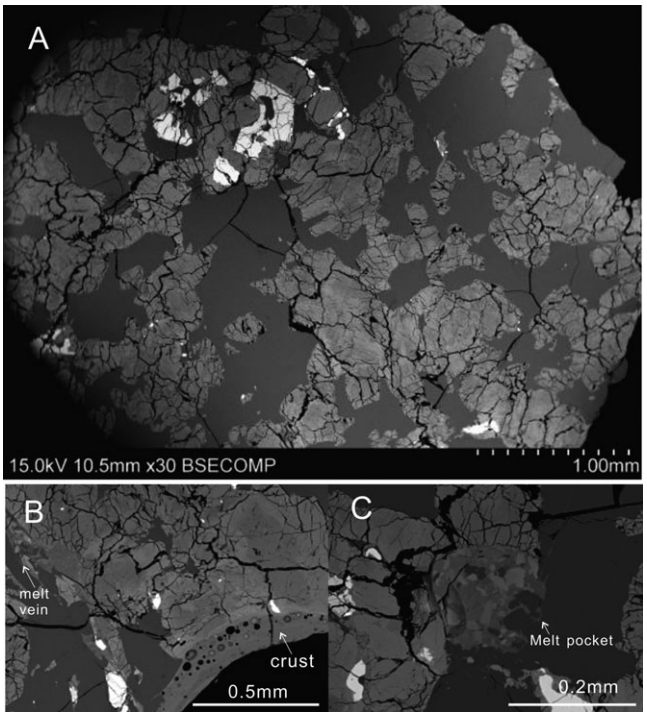

Fig. 1. Backscattered electron (BSE) images of NWA 2975 petrographic features. A) Image of the thick section. B and C) Images of fusion crust and shock features (melt pocket and veins) that are pervasive in the section. The vesicular gray area at the top of the section is the fusion crust. Vesicles (black circular regions) are heterogeneously distributed throughout the melted area. B) shows the fusion crust is a few of heterogeneous.

Based on our detailed SEM examination and point counting, NWA 2975 is composed predominantly of pyroxenes (56.0 vol%) and completely maskelynitized plagioclase (39.3 vol%) with accessory opaque phases (2.7 vol%) and phosphates (2.0 vol%). The melt pockets and melt veins are not included in the calculation. Our observation is consistent with the results provided by Wittke et al. (2006) on a separate thin section of NWA 2975 (57.3% pyroxenes, 38.3% maskelynites, 2.7% Fe-Ti oxides, and 1.7% phosphates). We obtained about 200 microprobe analyses on our polished section. Representative analyses of the various mineral phases are given in Tables 1-4.

Pyroxenes in NWA 2975 have a wide range of compositions, with both augite and pigeonite present (Table 1). The pyroxene compositional zoning (Fig. 2) is complex and distinct from that observed in Shergotty and QUE 94201. This complex zoning may be described

Table 1. Representative electron microprobe analyses (EMP) (in wt%) of pyroxene and maskelynite in NWA 2975.

	Pyroxene					Maskelynite	
Minerals	Pgn	Fe-Pgn	Aug	MI-Pgn	Minerals	Pl	Kf
SiO_2	51.1	45.7	51.6	47.5	SiO_2	56.1	63.9
TiO_2	0.24	0.5	0.31	0.54	TiO2	0.06	0.3
Al_2O_3	0.7	0.56	1.26	0.26	Al_2O_3	26.5	20.6
Cr_2O_3	0.08	–	0.26	–	Cr_2O_3	–	–
FeO	25.7	46.5	17.1	41.8	FeO	0.46	0.78
MnO	0.72	1.22	0.51	0.98	MnO	–	0.01
MgO	15.4	2.59	14.6	6.86	MgO	0.13	0.03
CaO	5.56	2.71	13.5	1.69	CaO	10.5	3.34
Na_2O	0.08	–	0.17	–	Na_2O	5.24	3.79
K_2O	<0.05	<0.05	<0.05	0.06	K_2O	0.18	6.54
P_2O_5	0.03	0.02	0.04	0.03	P_2O_5	0.02	–
Total	99.7	99.8	99.3	99.8	Total	99.2	99.4
Si	1.977	1.961	1.968	1.977	Si	2.549	2.891
Ti	0.007	0.016	0.009	0.017	Ti	0.002	0.014
Al	0.032	0.028	0.057	0.013	Al	1.415	1.099
Cr	0.003	–	0.008	–	Cr	–	–
Fe^T	0.833	1.667	0.544	1.455	Fe^T	0.017	0.03
Mn	0.024	0.044	0.017	0.034	Mn	–	–
Mg	0.889	0.165	0.830	0.426	Mg	0.009	0.002
Ca	0.231	0.124	0.550	0.075	Ca	0.512	0.162
Na	0.006	–	0.013	–	Na	0.462	0.33
K	–	–	–	0.003	K	0.010	0.38
P	0.001	0.001	0.001	0.001	P	0.001	–
Total	4.001	4.008	3.996	4.000	Total	4.977	4.904
Fe/Mn	35.1	37.6	32.7	42.3	An	52.0	18.5
En	45.6	8.4	43.2	21.8	Ab	46.9	38.2
Fs	42.6	85.2	28.3	74.4	Or	1.0	43.3
Wo	11.8	6.4	28.6	3.9			

Pgn = pigeonite; Fe-Pgn = extreme Fe-rich pigeonite; Aug = augite; MI-Pgn = pigeonite within melt inclusion; Pl = plagioclase; Kf = K-feldspar.

Table 2. Representative electron microprobe analyses (EMP) (in wt%) of glasses and merrillites from NWA 2975.

	NWA 2975					NWA 2975		Shergotty	Los Angeles	EETA79001
Samples	Gl	Q	K-Gl	K-Gl	Samples	mer	mer	mer	mer	mer
SiO_2	70.9	97.6	77.1	78.5	SiO_2	0.24	0.18	0.12	0.11	0.1
TiO_2	0.15	0.15	0.26	0.69	TiO_2	0.05	–	–	–	–
Al_2O_3	17.8	1.18	11.6	11.1	Al_2O_3	0.02	0.04	0.03	–	<0.02
Cr_2O_3	–	–	–	–	Cr_2O_3	0.03	0.04	–	–	–
FeO	0.51	0.44	0.95	0.73	FeO	3.45	3.67	4.21	4.96	4.97
MnO	–	–	0.08	0.07	MnO	0.12	0.16	0.16	–	<0.04
MgO	0.05	0.01	–	–	MgO	2.09	1.83	1.44	0.91	1.25
CaO	4.91	0.08	0.64	0.60	CaO	46.4	46.3	46.2	46.9	46.2
Na_2O	5.01	0.44	1.74	1.82	Na_2O	1.32	1.47	1.27	1.2	0.72
K_2O	0.33	0.18	7.36	6.92	K_2O	0.06	0.05	–	–	–
P_2O_5	0.02	–	0.11	0.09	P_2O_5	45.7	45.7	44.4	44.9	45.6
Total	99.7	100.1	99.9	100.6	Cl	–	–			
					F	0.87	0.67			
					Total	100.4	100.2	97.8	99.0	98.8

Gl = glass; Q-SiO_2 = rich glass; K-Gl = K-rich glass; mer = merrillite. Merrillites in Shergotty are after Lundberg et al. (1988), merrillites in Los Angeles are after Greenwood et al. (2003), and in EETA79001 are after Steele and Smith (1982).

Table 3. Representative electron microprobe analyses (EMP) (in wt%) of Fe-Ti oxides from NWA 2975.

Minerals	Ulvöspinel					Minerals	Ilmenite		
Spots no.	1	2	5	6	7	Spots no.	1	2-1	2-2
SiO_2	0.14	0.17	0.19	0.14	0.16	SiO_2	0.12	0.10	0.12
TiO_2	25.3	25.0	23.9	25.4	24.3	TiO_2	51.3	51.0	51.6
Al_2O_3	1.67	1.95	1.62	1.79	1.79	Al_2O_3	0.09	0.10	0.05
Cr_2O_3	0.68	0.67	–	1.1	0.25	Cr_2O_3	0.04	–	–
FeO	69	69.5	71.8	69	70.9	FeO	46	46.3	46.1
MnO	0.59	0.57	0.59	0.49	0.5	MnO	0.57	0.55	0.64
MgO	0.39	0.47	0.11	0.47	0.36	MgO	0.73	0.58	0.52
CaO	–	–	–	–	0.02	CaO	–	–	0.06
Na_2O	0.05	–	–	0.01	–	Na_2O	0.02	–	–
K_2O	–	0.01	0.01	–	–	K_2O	–	–	0.02
Total	97.8	98.3	98.3	98.3	98.3	Total	98.9	98.7	99.0
Si	0.006	0.007	0.008	0.006	0.006	Si	0.003	0.003	0.003
Ti	0.754	0.741	0.720	0.750	0.727	Ti	0.984	0.983	0.988
Al	0.078	0.091	0.077	0.083	0.084	Al	0.003	0.003	0.002
Cr	0.021	0.021	–	0.034	0.008	Cr	0.001	–	–
Fe^T	2.287	2.292	2.403	2.268	2.358	FeT	0.980	0.992	0.981
Mn	0.020	0.019	0.020	0.016	0.017	Mn	0.012	0.012	0.014
Mg	0.023	0.028	0.007	0.028	0.021	Mg	0.028	0.022	0.020
Ca	–	–	–	–	0.001	Ca	–	–	0.002
Na	0.004	–	–	0.001	–	Na	0.001	–	–
K	–	–	–	–	–	K	–	–	0.001
Total	3.192	3.198	3.234	3.186	3.221	Total	2.011	2.014	2.009
$MgAl_2O_4$	3.7	4.4	3.8	4.1	4.1	$MgTiO_3$	2.6	2.1	1.9
$FeCr_2O_4$	0.6	0.5	0	0.9	0.2	$FeTiO_3$	94.2	94	95.8
Fe_2TiO_4	72.1	71.4	72	70.5	71.7	Fe_2O_3	3.1	3.9	2.3
$FeFe_2O_4$	23.1	23.3	24	23.6	23.8				

$Fe_2TiO_4 = 100*2Ti/(2Ti + Cr + Al + Fe^{3+})$; $FeFe_2O_4 = 100*Fe^{3+}/(2Ti + Cr + Al + Fe^{3+})$; $FeCr_2O_4 = 100*Cr/(2Ti + Cr + Al + Fe^{3+})$; $MgAl_2O_4 = 100*Al/(2Ti + Cr + Al + Fe^{3+})$.

as a "chaotic" or "patchy" texture similar to that described in Martian meteorite NWA 8679 (see Fig. 2A and 2B; Tait et al. 2015). The Mg-rich augite and Mg-rich pigeonite cores have late-stage overgrown, Fe-rich pigeonite rims (Fig. 2C). Both Mg-rich pigeonite and the Fe-rich pigeonite rims typically contain exsolution features in the form of very thin, 0.2–0.5 μm wide orthopyroxene exsolution lamellae (Fig. 2C). Late-stage pyroxenes, which commonly occur within large maskelynite areas, are extremely Fe-rich (Fs_{83-86} Wo_{6-8}, Fig. 2D, Fig. 3, and Table 1).

EMP analyses reveal two distinct pyroxene compositional trends: a pigeonite trend ranging from $Fs_{43}Wo_{12}$to $Fs_{63}Wo_{17}$ and an augite trend ranging from $Fs_{23}Wo_{36}$ to $Fs_{49}Wo_{27}$. Figure 3 shows that NWA 2975 pyroxenes have compositional trends similar to those observed in Shergotty, Zagami, NWA 856, and NWA 3171 (Stolper and McSween 1979; Stöffler et al. 1986; McCoy et al. 1992; Jambon et al. 2002; Irving et al. 2004). However, the augite and pigeonite cores of NWA 2975 are Fe-rich compared to those in most other basaltic shergottites with the exception of Los Angeles and Dhofar 378 (Sanborn and Wadhwa 2010). Fe/Mn (molar) ratios of pyroxenes have been used successfully to categorize planetary basalts (Papike 1998; Papike et al. 2003). NWA 2975 pigeonites have Fe/Mn = 35–41 and augites have Fe/Mn = 30–39, consistent with average SNC pyroxenes (Papike et al. 2003).

Plagioclases have entirely been converted to maskelynite and cluster tightly near a composition of $An_{52-55}Or_1$ (Table 1), in agreement with maskelynite compositional trends seen in other shergottites such as Shergotty (Stolper and McSween 1979) and Los Angeles (Rubin et al. 2000). A few K-feldspars have been observed ($An_{19}Or_{43}$, Table 1). However, the feldspar or feldspathic glass in the mesostasis regions of NWA 2975 is more variable in composition and part of it is enriched in K (An_5Or_{68}, Table 2).

Accessory phases include phosphates, Fe-Ti oxides, sulfides, Si-Al-K-Na-rich glass, and baddeleyites. All the phosphate present in NWA 2975 is merrillite. It occurs as small interstitial laths (about 150 μm length for the largest grain) adjacent to or intruding Fe-rich clinopyroxene and/or Fe-Ti oxides (Fig. 4). Based on

Table 4. Representative electron microprobe analyses (EMP) and LA-ICP-MS analyses (in wt%) of fusion crust and shocked veins.

Samples	Crust					Av Crust1	Av Crust2	Av Crust3	Crust		Av Crust (n = 10)	SD
Methods	EMP	EMP	EMP	EMP	EMP	EMP	EMP	EMP	LA-ICP-MS (1σ)	LA-ICP-MS (1σ)	LA-ICP-MS	LA-ICP-MS
SiO_2	51.6	48.8	51.6	49.2	50.4	49.9	49.7	49.3	48.7 (0.63)	49.7 (0.83)	49.1	0.82
TiO_2	0.67	0.99	0.54	0.89	0.6	0.68	0.74	0.78	0.82 (0.01)	0.69 (0.02)	0.67	0.11
Al_2O_3	2.06	5.59	10.4	5.3	7.57	6.96	7.00	6.80	8.58 (0.14)	9.3 (0.18)	9.16	0.63
Cr_2O_3	0.13	0.02	0.17	0.22	0.03	0.11	0.14	0.10	0.13 (0.01)	0.12 (0.01)	0.12	0.01
FeO	21.0	20.2	14.5	19.4	16.4	17.2	18	18.1	18.6 (0.23)	17.2 (0.30)	17.5	0.9
MnO	0.59	0.45	0.4	0.46	0.37	0.45	0.45	0.46	0.46 (0.01)	0.46 (0.01)	0.46	0.02
MgO	9.54	7.69	7.48	8.12	8.29	8.00	7.70	8.16	8.03 (0.11)	7.85 (0.15)	8.07	0.23
CaO	11.5	12.8	10.9	13.1	11.3	11.3	12.5	11.9	12.3 (0.22)	12.3 (0.26)	12.5	0.43
Na_2O	0.68	1.25	1.66	1.22	1.38	1.36	1.50	1.49	1.58 (0.02)	1.65 (0.03)	1.64	0.12
K_2O	0.03	0.13	0.09	0.13	0.07	0.09	0.10	0.10	0.09 (0.00)	0.09 (0.00)	0.09	0.01
P_2O_5	0.18	1.64	0.46	1.71	0.43	0.65	0.99	–	0.69 (0.01)	0.57 (0.01)	0.55	0.12
Total	97.9	99.6	98.3	99.8	96.9	96.8	98.8	97.2	100	99.9	100	

Samples	Vein										
Methods	EMP	EMP	EMP	EMP	LA-ICP-MS	LA-ICP-MS	LA-ICP-MS	Shergotty	Zagami	Los Angeles	B-S WR av (1σ)
SiO_2	46.5	46.2	50.0	50.8	50.2	50.6	56.3	50.4	50.8	48.5	49.9 (1.24)
TiO_2	2.30	2.18	0.41	1.45	0.35	0.89	0.21	0.81	0.77	1.35	1.22 (0.41)
Al_2O_3	4.34	3.06	0.94	7.49	3.02	10.7	22.4	6.89	5.67	10.6	8.75 (2.63)
Cr_2O_3	0.06	0.07	0.05	0.05	0.23	0.04	0.01	0.21	0.3	0.01	–
FeO	27.9	28.9	26.1	22.3	19.5	18.7	4.75	19.1	18	21.4	19 (1.36)
MnO	0.69	0.72	0.82	0.52	0.47	0.46	0.09	0.5	0.5	0.49	0.48 (0.03)
MgO	8.54	9.47	14	5.28	13	6.77	1.55	9.27	11	3.73	7.71 (2.91)
CaO	7.54	7.43	6.63	8.8	12.5	8.25	8.93	10.1	10.8	9.9	10.3 (0.77)
Na_2O	1.09	0.57	0.1	1.57	0.45	2.32	4.97	1.37	0.99	2.17	1.55 (0.41)
K_2O	0.13	0.12	-	0.15	0.09	0.19	0.38	0.16	0.14	0.3	0.13 (0.07)
P_2O_5					0.13	1.00	0.30			1.5	0.11
Total	99.0	98.8	99.0	98.4	99.9	99.9	100			99.9	

Av Crust (n = 10) is the 10 analyses of the crust by LA-ICP-MS. SD is the standard deviation of the samples.

For comparison, the whole rock composition of Shergotty and Zagami are shown after Stolper and McSween (1979), and the whole rock composition of Los Angeles is after Rubin et al. (2000).

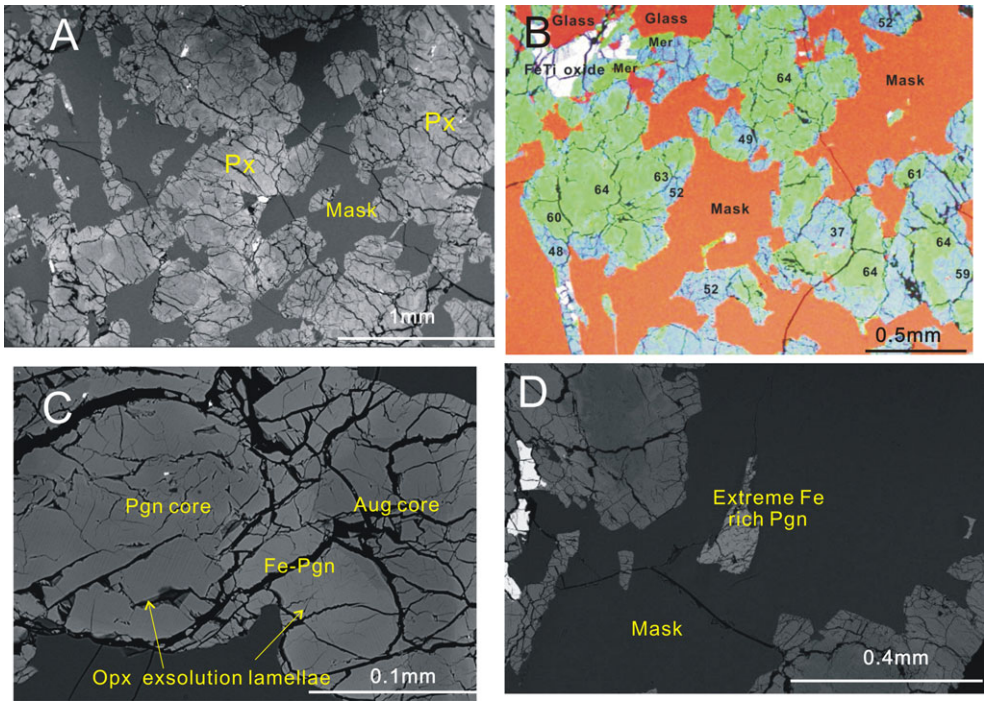

Fig. 2. Photomicrographs illustrating textures of the pyroxenes in NWA 2975(A–D). A) BSE image showing weak preferred orientation of pyroxenes and maskelynite grains. Pyroxenes are medium to light gray. B) False color image of combined X-ray Ca (green)-Fe (blue)-Al (red). The numbers shown are the Mg# number of the pyroxenes. C) Mg-rich augite and Mg-rich pigeonite were surrounded by Fe-rich pigeonite. Both Fe-rich pigeonite grains and Mg-rich pigeonite grains contain thin exsolution lamellae. D) Extreme Fe-rich pigeonite occurred within the large maskelynite grains. Aug = augite; Ferro-Pgn = Fe-rich pigeonite; Aug core = Mg-rich augite; Pgn core = Mg-rich pigeonite; Extreme Fe-pgn = extremely Fe-rich pyroxene.

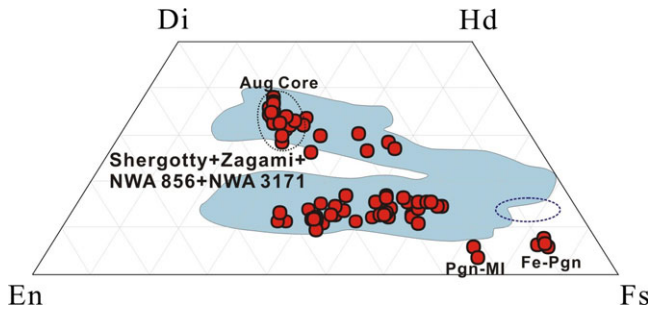

Fig. 3. Pyroxene compositions in NWA 2975 compared with those in other evolved basaltic shergottites (data for Shergotty, Zagmai, NWA 856, and NWA 3171 are from Stöffler et al. [1986], Stolper and McSween [1979], McCoy et al. [1992], Jambon et al. [2002], and Irving et al. [2004]). The ellipse outlines the range of lunar pyroxferroite (Aramovich et al. 2002). Px-MI, pyroxene grains within melt inclusions. Ferro-Pgn = Fe-rich pigeonite; extreme Fe-px = extremely Fe-rich pyroxene.

about 20 analyzed laths, the merrillites contain more MgO (1.8–2.3 wt%) but less FeO (3.2–3.9 wt%) than phosphates in other basaltic shergottites (Shergotty, Los Angeles, EETA79001; see Table 2). Their Cl and F abundances are 0.01 wt% and 0.67–0.95 wt%, respectively.

NWA 2975 contains some trapped melt inclusions in large, Fe-rich pigeonite or Fe-Ti oxide grains (Figs. 4A–C). These melts exhibit rims of Fe-rich pigeonite + merrillite surrounding cores of Si-Al-K-Na-rich glass (Fig. 4B). Our analyses show that these Fe-Ti oxides are actually Ti-magnetite, not "ulvöspinel" as reported by a previous study (Table 3, Wittke et al. 2006). These Ti-magnetites are relatively homogeneous in composition, enriched in TiO_2 (22–25 wt%), low in Al_2O_3 (1.6–2 wt%) and Cr_2O_3 (0–1 wt%), and consistent with a formula of $Usp_{71\text{-}72}Mt_{23\text{-}24}Sp_4Chr_{0\text{-}1}$ (Usp = molar $100*2Ti/[2Ti + Cr + Al + Fe^{3+}]$; Mt = molar $100*Fe^{3+}/[2Ti + Cr + Al + Fe^{3+}]$; Chr = molar $100*Cr/[2Ti + Cr + Al + Fe^{3+}]$; Sp = molar $100*Al/[2Ti + Cr + Al + Fe^{3+}]$; defined in Goodrich 2003; Table 3). Ilmenite is always attached to Ti-magnetite as an exsolution product (Fig. 4D). Ilmenite grains are nearly pure $FeTiO_3$ with the formula of $Ilm_{94\text{-}96}$.

Fine, symplectitic intergrowths composed of fayalite + silica + Fe-Ti oxides + phosphate occur as inclusions within maskelynite, although they are rare in this sample (Fig. 5A). Such texture is similar to the symplectitic assemblage of fayalite + silica + ferro-pyroxene found in Los Angeles meteorite (possibly

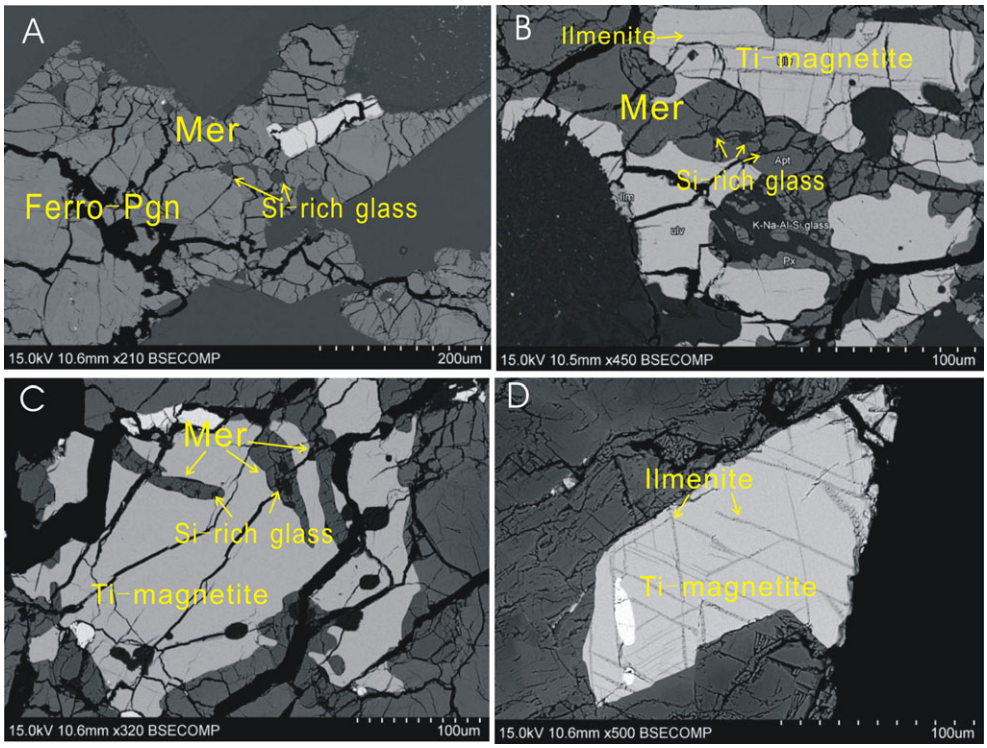

Fig. 4. Petrographic features of phosphates and Fe-Ti oxides in NWA 2975. A) phosphate (Mer) and Si-rich melts intruded in grains Fe-rich pigeonite (Ferro-Pgn). B and C) Trapped melt inclusions or phosphate and Si-rich melts intruded in grains of Fe-Ti oxides. The melts exhibit marginal rims of Fe-rich pigeonite + merrillite surrounding cores of Si-Al-K-Na-richglass in image (B). D) Ti-magnetite grains have ilmenite exsolution lamellae.

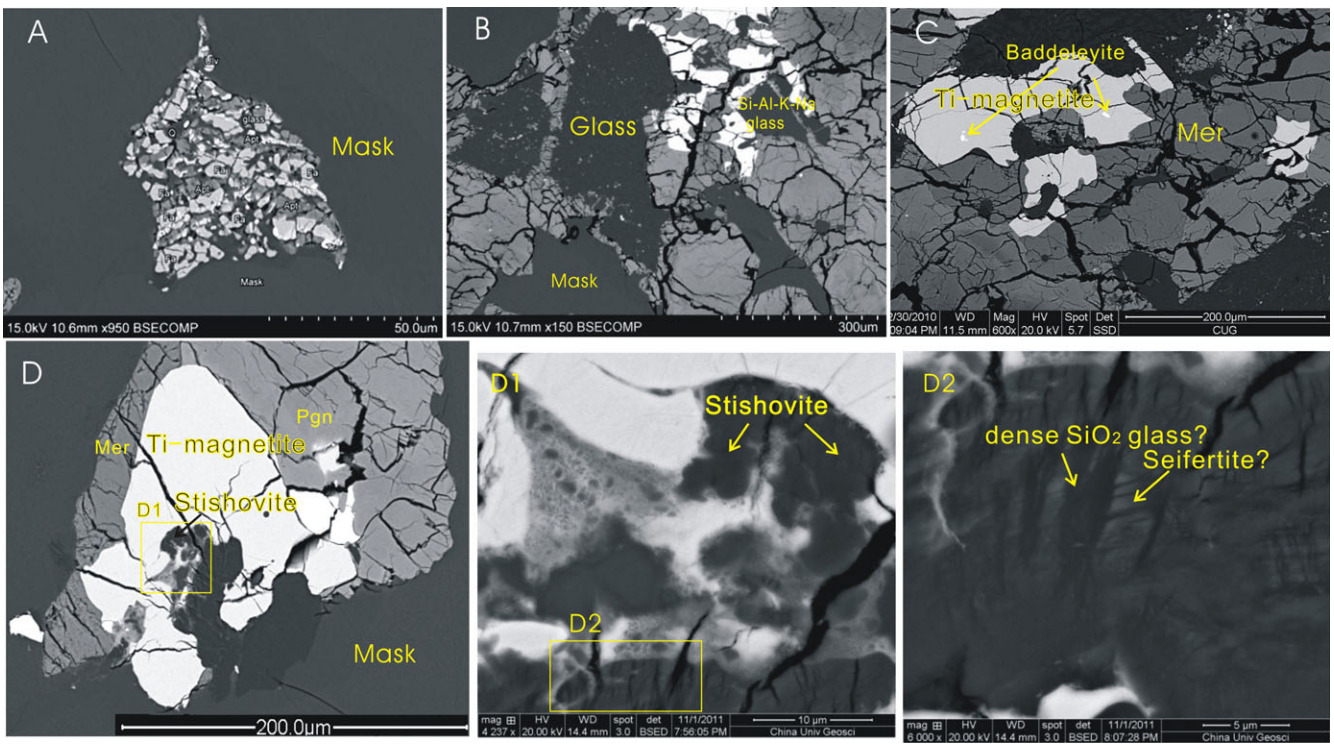

Fig. 5. BSE images of silica, silica-rich glass, and other accessory phases in NWA 2975.

formed after pyroxferroite; Aramovich et al. 2002; Warren et al. 2004). Here, these symplectitic intergrowths might have formed as late-stage mesostasis. Silica-rich glasses are present as gap fillings between the laths of plagioclase/pyroxene and Fe-Ti oxides in the mesostasis, which are late-stage Si-Al-K-Na-rich glasses and mixed glasses (Figs. 5B and 5C). Some nearly pure SiO_2 glasses (with about 1 wt% Al_2O_3) were observed associated with maskelynitic glasses (Fig. 5D).

Iron sulfides (probably pyrrhotite) are present in the mesostasis or as rare inclusions within Ti-magnetite. Identified baddeleyite grains are commonly located near the regions of amorphous glass or associated with Fe-Ti oxides and maskelynite, while others also occur as inclusions within the Fe-Ti oxides (see Figs. 5C and 6 for baddeleyite's characteristic Raman spectrum). The baddeleyite grains are approximately rectangular and extremely small, with the largest measuring ~10 μm × 2 μm. Only six baddeleyite grains were found in the mesostasis, and most of these grains are too small for full characterization (about 3 μm).

Amorphous silica occurs as irregular grains between plagioclase, clinopyroxene, and Fe-Ti oxides (Fig. 5D). Within the amorphous silica, stishovite (which has been reported previously in Martian meteorites, e.g., Sharp et al. 1999; Langenhorst and Poirier 2000; Beck et al. 2004, 2005; Baziotis et al. 2013) was identified by its characteristic Raman intense peak at 756 cm^{-1} and the minor peak at 239 cm^{-1} (Hemley et al. 1986; El Goresy et al. 2004; see Figs. 5D1 and 6 for Raman spectrum); the peak at 612 cm^{-1} probably is associated with the surrounding Fe-oxide (Wang et al. 2004a). There are white and black lamellae intergrowing with each other in the amorphous silica as shown in BSE image (Fig. 5D2). No compositional differences were detected between white and black lamellae. They are conceivably shock-induced and will be discussed later.

REE Geochemistry

In situ REE analyses were carried out on pyroxene, maskelynite, merrillite, and the fusion crust of NWA 2975. Representative SIMS REE data for minerals and glasses are given in Table 5. The REE abundances of pigeonite, augite, and maskelynite are low (~0.1 × CI chondrites), while merrillite has the highest REE abundance (up to hundreds of times CI chondrites, Fig. 7).

Augite has higher REE abundances than pigeonite. Both augite and pigeonite are characterized by LREE-depleted patterns [$(La/Yb)_{CI}$ = 0.02–0.03 for pigeonite versus $(La/Yb)_{CI}$ = 0.05–0.08 for augite] with small negative to positive Eu anomalies (Eu*/Eu = 0.6–1.3)

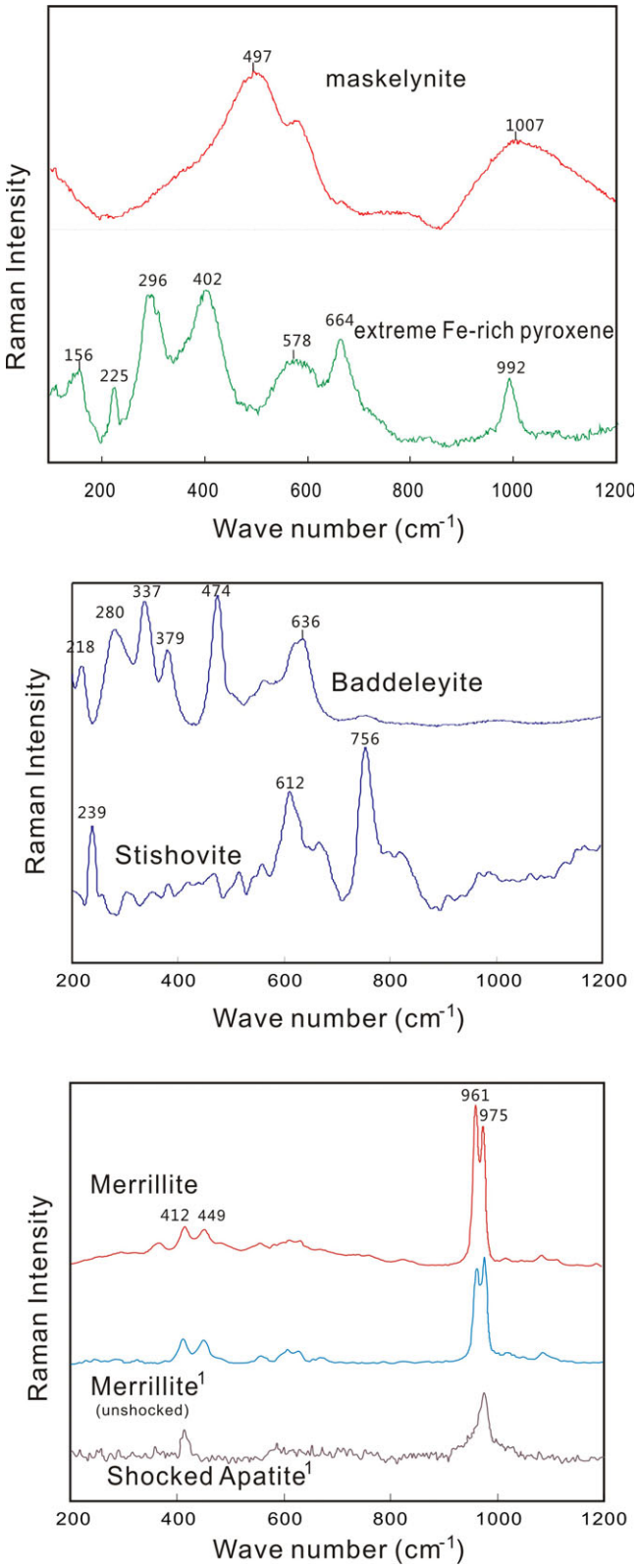

Fig. 6. Raman spectra of maskelynite, extreme Fe-rich pyroxene, baddeleyite, stishovite, and merrillite in NWA 2975. For comparison, Merrillite[1] and shocked apatite[1] after Wang et al. (2004b) for Martian shergottites are shown.

Table 5. Representative trace element compositions (in ppm) of minerals and fusion crust for NWA 2975.

Samples	Pgn En42Wo13 (σ)	Aug En41Wo35 (σ)	Pl An54 (σ)	Samples	Mer Mer (σ)	Crust SIMS (σ)	Crust LA-ICP-MS (σ)	Crust Av Crust (n = 10)	SD
Sc	66.1 (0.3)	109 (1)	10.9 (0.1)	Sc	150 (2)	75.5 (0.4)	63.3 (1.4)	61.5	0.2
Ti	1249 (7)	1554 (9)	187 (3)	Ti	46601 (153)	4164 (16)	4615 (77)	4014	659
V	195 (1)	448 (1)	5.70 (0.15)	V	709 (5)	263 (1)	309 (5)	302	1
Ni	352 (5)	483 (7)	169 (4)	Ni	985 (29)	360 (6)	63 (3)	59	1
Rb	20.4 (0.6)	9.67 (0.46)	0.439 (0.093)	Rb	235 (7)	13.2 (0.6)	3.52 (0.30)	2.39	0.9
Sr	3.11 (0.11)	3.49 (0.14)	122 (1)	Sr	254 (4)	50.7 (0.6)	58.8 (2.0)	70.8	15
Y	3.51 (0.05)	7.584 (0.083)	0.114 (0.010)	Y	613 (2)	22.3 (0.2)	19.6 (0.6)	16.5	3.6
Zr	1.71 (0.05)	4.281 (0.100)	0.037 (0.009)	Zr	661 (4)	44.3 (0.4)	44.2 (2.0)	36.6	8.8
Ba	3.82 (0.06)	0.917 (0.036)	11.6 (0.1)	Ba	283 (2)	16.2 (0.2)	22.9 (1.5)	22.7	10.5
La	0.017 (0.003)	0.087 (0.009)	0.106 (0.010)	La	109 (1)	2.86 (0.06)	2.45 (0.17)	1.90	0.5
Ce	0.079 (0.008)	0.358 (0.019)	0.155 (0.012)	Ce	237 (2)	6.83 (0.09)	5.91 (0.22)	4.73	1.4
Pr	0.013 (0.003)	0.078 (0.008)	0.022 (0.004)	Pr	36.5 (0.5)	1.00 (0.03)	0.85 (0.07)	0.7	0.2
Nd	0.117 (0.013)	0.653 (0.038)	0.073 (0.012)	Nd	200 (2)	5.06 (0.12)	4.10 (0.41)	3.41	0.7
Sm	0.097 (0.019)	0.349 (0.043)	0.011 (0.008)	Sm	87.4 (2.1)	2.20 (0.12)	1.99 (0.23)	1.45	0.4
Eu	0.063 (0.026)	0.238 (0.054)	0.351 (0.087)	Eu	28.5 (2.1)	0.98 (0.14)	0.75 (0.08)	0.62	0.2
Gd	0.261 (0.023)	0.782 (0.054)	0.031 (0.009)	Gd	114 (2)	3.16 (0.10)	3.15 (0.27)	2.37	0.6
Tb	0.080 (0.008)	0.183 (0.014)	0.007 (0.003)	Tb	18.5 (0.4)	0.61 (0.03)	0.48 (0.06)	0.43	0.1
Dy	0.568 (0.023)	1.428 (0.045)	0.018 (0.004)	Dy	138 (1)	4.16 (0.09)	2.99 (0.28)	2.80	0.7
Ho	0.151 (0.011)	0.345 (0.019)	0.008 (0.003)	Ho	25.2 (0.5)	0.87 (0.03)	0.81 (0.06)	0.60	0.2
Er	0.431 (0.020)	0.880 (0.033)	0.011 (0.004)	Er	66.3 (0.9)	2.58 (0.06)	2.29 (0.18)	1.89	0.4
Tm	0.062 (0.007)	0.135 (0.011)	0.001 (0.003)	Tm	10.3 (0.3)	0.36 (0.02)	0.30 (0.05)	0.26	0.1
Yb	0.611 (0.041)	0.806 (0.058)	0.007 (0.006)	Yb	55.1 (1.5)	2.55 (0.11)	2.08 (0.23)	1.63	0.4
Lu	0.070 (0.008)	0.111 (0.013)	–	Lu	6.48 (0.33)	0.34 (0.03)	0.24 (0.03)	0.22	0.037
Hf	6.68 (5.60)	–	–	Hf	–	–	1.25 (0.16)	1.10	0.3
Eu/Eu*	1.1	1.3	–	Th	1.85 (0.23)	–	0.40 (0.05)	0.32	0.1
La/Yb_{CI}	0.02	0.08	–	U	1.92 (0.30)	–	0.20 (0.04)	0.12	0.1

Pgn = pigeonite; Aug = augite; Pl = plagioclase; Mer = merrillite; Av Crust (n = 10) is the 10 analysis of the crust by LA-ICP-MS. SD is the standard deviation of the crust by LA-ICP-MS.

($Eu^*/Eu = 2*Eu_{CI}/[Sm_{CI} + Gd_{CI}]$) (Fig. 7). The Eu anomalies suggest that the pyroxenes crystallized prior to or at the same time as plagioclase. Few pyroxenes have negative Ce anomalies, consistent with weak terrestrial weathering (Fig. 7, Wadhwa et al. 1994; Hsu et al. 2004). Within individual pyroxene, the REE patterns are similar for both the cores and the rims. The augite REE patterns and abundances are within the range of those observed in Shergotty and Zagami (Wadhwa et al. 1994; McCoy et al. 1999), whereas pigeonites are systematically enriched in REE abundances compared to the pigeonites from Shergotty and Zagami.

Maskelynites in NWA 2975 are moderately enriched in LREE with strong positive Eu anomalies (Fig. 7). The maskelynite REE patterns and abundances are similar to those in other enriched basaltic shergottites (Wadhwa et al. 1994; McCoy et al. 1999).

Merrillite in NWA 2975 has a flat REE pattern with a slightly negative Eu anomaly ($Eu^*/Eu = 0.78$; Fig. 7). Its REE pattern basically parallels those of other basaltic shergottite merrillites (Lundberg et al. 1990; McCoy et al. 1999; Wadhwa et al. 1994), albeit with slightly lower REE abundances.

Major and Trace Element Compositions of Fusion Crust and Shock Melt Veins

Due to the small sample amount available, the bulk chemical composition of NWA 2975 was not determined in this study. However, because fusion crust generally retains the overall geochemical compositions of basaltic meteorites, the average REE compositions of fusion crusts or even shock melt veins have been previously used as pseudobulk values (Gnos et al. 2002; Day et al. 2006; Wang et al. 2012). Several authors (e.g., Gnos et al. 2002; Day et al. 2006) have used the average of a few fusion crust analyses to approximate the bulk composition of the meteorites. However, this value must be used with caution (Thaisen and Taylor 2009) as fusion crusts are heterogeneous and limited analyses can give biased results.

Despite these issues, given the lack of available material, fusion crusts offered our only method to

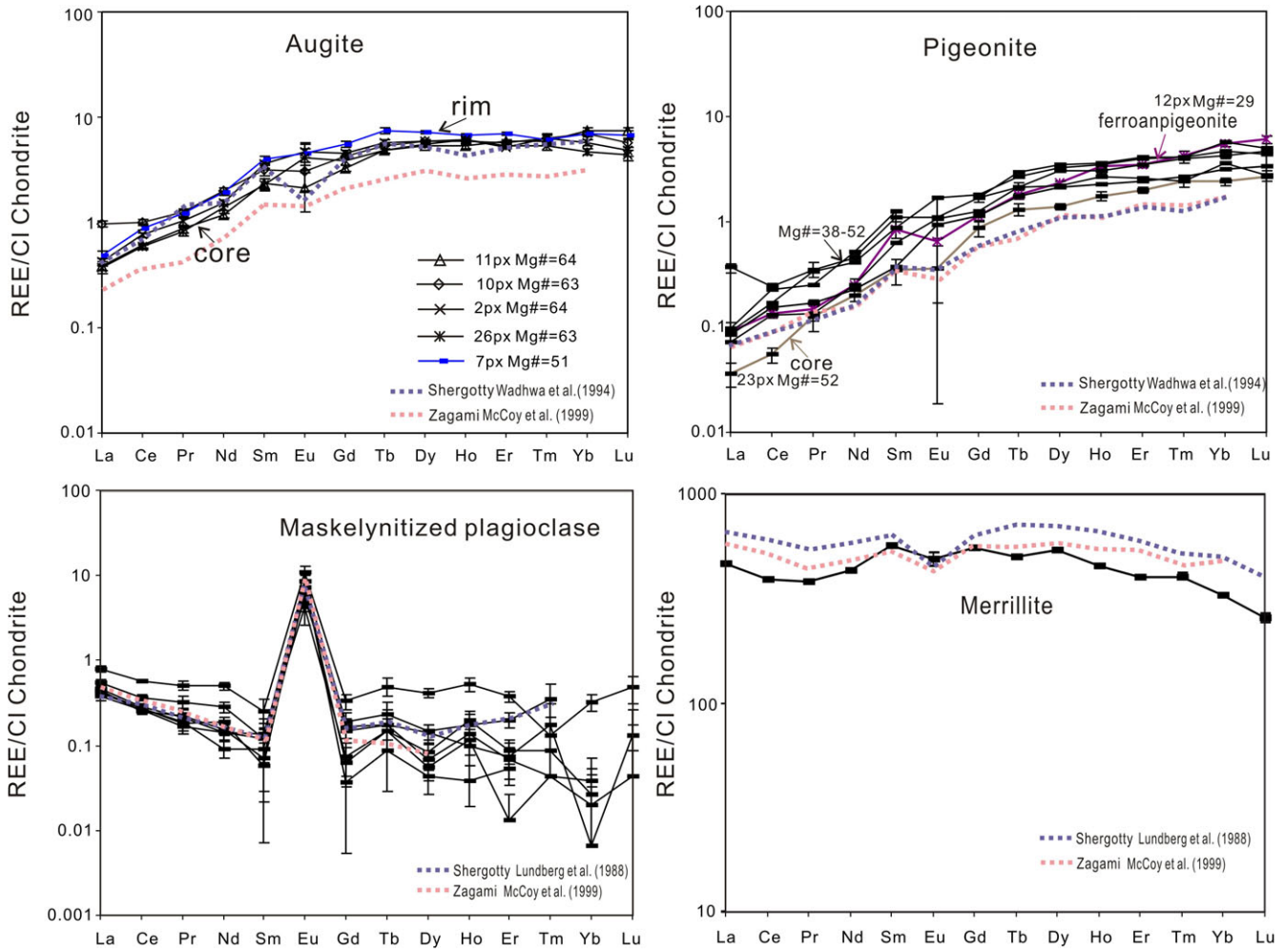

Fig. 7. Representative REE concentrations of pyroxenes, maskelynite, and merrillite of NWA 2975. For comparison, the mineral compositions of Shergotty and Zagami are shown after Wadhwa et al. (1994) and McCoy et al. (1999).

produce an estimated bulk composition that could be used to assess the relationship between this sample and other shergottites and the possibility of crustal assimilation during crystallization. Therefore, we present the results of those fusion crust measurements in addition to detailed characterization of the variance and attempt to use these analyses given appropriate care and consideration of other available data. First, we performed three EMP traverses through the fusion crusts at different locations to estimate major element heterogeneity due to nearby minerals; a major source of the heterogeneity characterized by Thaisen and Taylor (2009). The fusion crust compositions adjacent to plagioclase and pyroxene substrates range between these two endmembers. The averages of three traverses are similar to each other in their FeO + MgO, Al_2O_3, and most other element abundances. Fusion crust EMP analyses yielded the following average compositions (wt %): 50.8 SiO_2, 18.1 FeO, 7.13 Al_2O_3, 12.1 CaO, 8.13 MgO, 0.46 MnO, 0.75 TiO_2, 1.49 Na_2O, 0.10 K_2O, 0.12 Cr_2O_3, and 0.76 P_2O_5 (Table 4 and Tables S1–S3).

As the variance in the EMP spot analyses on fusion crust is high, we conducted LA-ICP-MS (11) analyses on larger areas of fusion crust to produce an additional composition estimate using an independent technique. The average value of major composition of the fusion crust measured by LA-ICP-MS is (wt%): 49.2 SiO_2, 17.5 FeO, 9.17 Al_2O_3, 12.5 CaO, 8.08 MgO, 0.46 MnO, 0.67 TiO_2, 1.64 Na_2O, 0.09 K_2O, 0.12 Cr_2O_3, and 0.55 P_2O_5 (Table 4). The LA-ICP-MS measurements show more homogeneous compositions than EMP analysis with small variation (Fig. 8). This measured composition is within error of the average of our fusion crust EMP analyses except for Al.

We also measured the composition of shock melt veins throughout the sample (6 LA-ICP-MS analyses). Our measurements show that the shock melt veins are more heterogeneous than the fusion crust (Table 4);

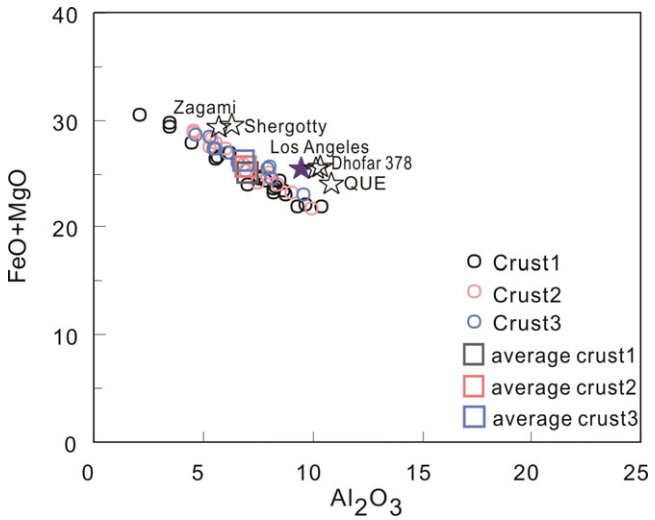

Fig. 8. EMP analyses of NWA 2975 indicating fusion crust compositional variations. FeO + MgO (pyroxene components) versus Al_2O_3 (plagioclase). The bulk compositions of other basaltic shergottites (i.e., Shergotty, Zagami, Los Angeles, Dhofar 378, and QUE 94201 are also plotted for comparison [Stolper and McSween 1979; Bridges and Warren 2006; Rubin et al. 2000; Ikeda et al. 2006]). The purple stars show LA-ICP-MS values of fusion crust.

some portions of the shock melt veins show depletion in Al (compared to the fusion crust measurements) while other portions show very low Mg, which may suggest that some locations are low in feldspathic components but dominated by pyroxene while in other locations the feldspathic component is dominant.

The average composition of NWA 2975 fusion crust is basaltic, comparable to the bulk rock compositions of other enriched basaltic shergottites (e.g., Shergotty and Zagami; Stolper and McSween 1979; Bridges and Warren 2006). The average Mg# (molar Mg/[Mg + Fe]) of the fusion crust is 0.44, similar to that of Shergotty, Zagami, and NWA 856 (Bridges and Warren 2006). There are large variations in P_2O_5 content (0.37–0.63 wt%) observed in various locations within the fusion crust, likely indicating variable degrees of melting for merrillite across the traverses. The fusion crust trends measured by EMP are systematically low in Al_2O_3 compared to the trend defined by the other samples (Fig. 8); however, the LA-ICP-MS analyses are elevated in Al_2O_3 compared to the EMP average suggesting that the EMP-measured mixing trends are systematically undersampling the maskelynite component. While we do not understand the origin of this low-Al_2O_3 EMP measurement, the LA-ICP-MS measurement is closer to the trend defined by the other enriched, basaltic shergottites and therefore is likely closer to representative of the NWA 2975 fusion crust composition for its Al_2O_3 content.

Trace element compositions of the fusion crust in NWA 2975 were measured using both SIMS and LA-ICP-MS techniques. As with the major elements, the application of two measurement techniques that operate at different spot sizes will allow us to better constrain the magnitude of fusion crust variation due to systematic oversampling of individual phases. The fusion crust measurements display larger magnitude variations than seen in major element chemistry (Tables 5 and S1–S3, Fig. 9), most likely again reflecting heterogeneous distribution and melting of merrillite, the major REE carrier in this meteorite (Day et al. 2006). Despite this variation, the REE patterns of the fusion crust are close to parallel to those of other "enriched" basaltic shergottites (Shergotty, Zagami, NWA 856, and NWA 3171), suggesting a consistency between the two measurement types and a direct connection between our measurements and Martian samples from a similar chemical class. However, we note that the REE abundances of the fusion crust measured by SIMS are systematically higher than those measured by LA-ICP-MS. This difference can be explained if merrillite is heterogeneously distributed and also on average oversampled by the SIMS analyses within the fusion crust. Furthermore, the lowest REE abundance SIMS measurements of fusion crust have positive Eu anomalies while the highest REE-abundance measurements have negative Eu anomalies, implying that some of the variation in SIMS-measured REE abundances between spots is driven by excesses of maskelynite in the low-REE areas and excesses of merrillite and maskelynite deficits in the high-REE areas. The REE patterns obtained by LA-ICP-MS analyses of fusion crust do not show as large of a compositional range as those of the SIMS analyses and the average LA-ICP-MS analyzed composition shows neither a positive nor a negative Eu anomaly, suggesting that the LA-ICP-MS measured compositions are the best-available estimate of the fusion crust REE abundances. The LA-ICP-MS fusion crust analyses partly overlap the SIMS analysis but extend to lower overall concentrations, suggesting that oversampling merrillite is a consistent issue with all of our fusion crust SIMS measurements, regardless of whether they have a positive or negative Eu anomaly. Finally, the average LA-ICP-MS measured REE abundances are parallel to and within error of those previously measured in NWA 3171, NWA 856, and Shergotty; all members of the enriched basaltic shergottite family (Fig. 9).

Meyer (2012) reported a bulk rock ICP-MS analysis of NWA 2986 (thought to pair with NWA 2975, Fig. 9) including selected elements. Interestingly, the REE patterns in NWA 2986 are not parallel to the bulk

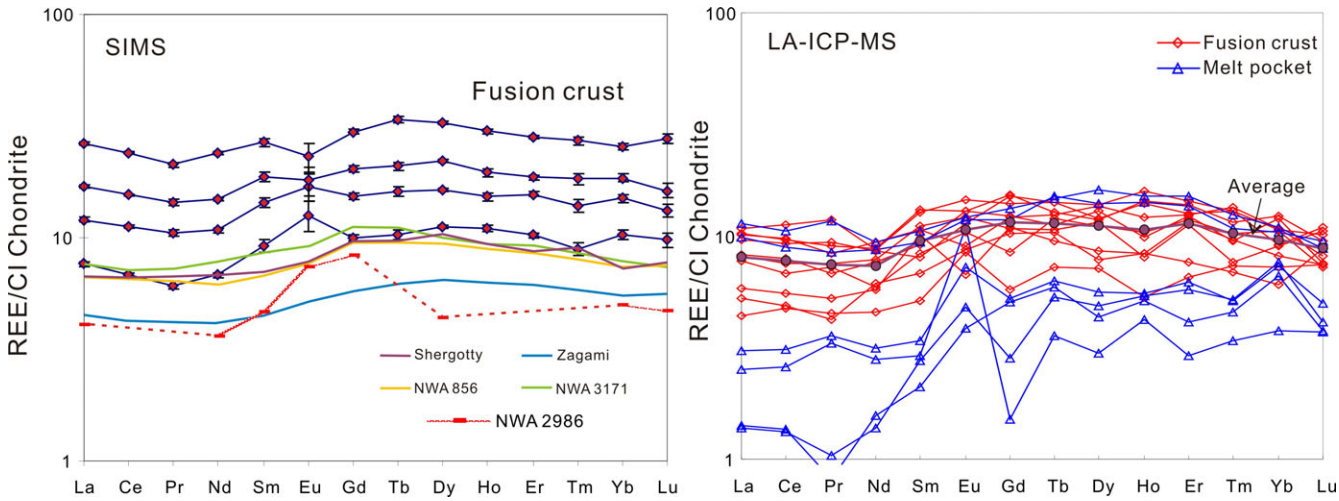

Fig. 9. Representative REE concentrations melt crust and melt pockets of NWA 2975 and comparison with abundances for "enriched" basaltic shergottites (data from Stolper and McSween 1979; McCoy et al. 1992; Jambon et al. 2002; and Irving et al. 2004).

analysis of NWA 856, NWA 3171, Zagami, or Shergotty; there are positive Eu and Gd anomalies and no increase in the abundances of middle-REE such as Dy reported for NWA 2968. If the select analyses of NWA 2986 are accurate, they could imply that the suggested pairing between NWA 2986 and NWA 2975 is incorrect; however, as the Eu-Gd bulk rock positive anomalies reported for NWA 2968 are not found in other enriched, basaltic shergottites these measurements need additional analyses for confirmation. If we instead focus on the published abundances for La, Nd, Yb, and Lu in NWA 2986, we see that those analyses closely overlap published bulk rock measurements for Zagami and are parallel to the other enriched, basaltic shergottites. Furthermore, our LA-ICP-MS analyses do approximately parallel those of the NWA 2986 whole rock, although NWA 2975 fusion crusts again display slightly higher REE abundances; possibly again either due to a lack of pairing or due to the use of fusion crust measurements in our case.

DISCUSSION

Shock Metamorphism and Its Side Effects

Shock features such as impact-melt veins and impact-melt pockets are ubiquitous within NWA 2975 (Fig. 1). Using Raman spectroscopy, we specifically identified the presence of "pyroxferroite" through comparison with previously reported Raman spectra of Martian pyroxferroite found in Dhofar 378 (peaks of 991, 658, 384, and 307 cm^{-1}; Ikeda et al. 2006) and a lunar triclinic pyroxenoid (Wang et al. 1997). Pyroxferroite occurs in some other shergottites, such as in QUE 94201 (McSween et al. 1996) and Los Angeles (fine-grained intergrowths of fayalite + ferroan augite + silica after breakdown of pyroxferroite; Warren et al. 2004). "Pyroxferroite" from NWA 2975 may have formed either from late-stage crystallization rimming ferroan pigeonite or a magma cooled rapidly enough to crystallize metastably; the latter case has been proposed for the pyroxferroite from QUE 94201 (McSween et al. 1996). Furthermore, experimental results on pyroxenoid formation suggested that pyroxferroite is only stable at pressures ≥ 1.0 GPa and temperatures >1030 °C (Lindsley and Burnham 1970); therefore, if pyroxferroite crystallizated from a basaltic magma (at or near surface), that could only have been metastably. Therefore, as long as in NWA 2975 "pyroxferroite" is mostly entrained within maskelynite, with the latter being formed after localized shock-heating, we may accept the hypothesis that pyroxferroite formed at high pressures with a cooling rate high enough to crystallize metastably as would be produced during shock. Furthermore, the presence of symplectite intergrowths (see the Petrography and Mineral Chemistry section) suggest a slow cooling rate which may facilitate pyroxferroite decomposition after the shock event (Lindsley et al. 1972; McSween et al. 1996).

Phosphate grains in shergottites have been suggested to have formed during crystallization (e.g., Wadhwa et al. 1994), later weathering (Bouvier et al. 2005), or shock processes (Chen et al. 1995; Wang et al. 2004b). The large phosphates in NWA 2975 exhibit crystallization textures and their REE patterns are parallel to those of the fusion crust, so they are unlikely

to have formed from or been influenced by terrestrial weathering processes. Additionally, the Raman spectrum of a merrillite grain in NWA 2975 (Fig. 6) displays an intense double peak at 961 and 975 cm^{-1} and two more, less-intense peaks at 412 and 449 cm^{-1}. A shocked apatite, first discovered by Chen et al. (1995) in shocked Sixiangkou (L6) chondrite has distinctively different Raman bands from unshocked apatite (the 962 cm^{-1} peak splits into three peaks, implying a distortion of the PO_4^{3-} tetrahedron). The differences in Raman spectra of shocked merrillite against the unshocked merrillite summarized are (1) the peak full width at half maximum (FWHM) decreased, (2) the peak intensities increased, and (3) the peaks are well-resolved (Chen et al. 1995; Fig. 6). Given such Raman spectra modifications, the NWA 2975 merrillite Raman spectrum closely resembles the unshocked merrillite similar to that reported by Wang et al. (2004b). Therefore, the Raman spectra of phosphates in NWA 2975 suggest an unshocked origin. Phosphate is typically among the last phases to crystallize in both Martian and lunar basaltic magmas, beginning crystallization after 75–90% of the initial melt has crystallized (McCubbin et al. 2012). The unshocked Raman signature might imply the merrillite formed after the meteorite was shocked or formed as a result of the shock melting process. Furthermore, the NWA 2975 phosphate peaks at 961 and 975 cm^{-1} are slightly shifted toward higher wave number compared to whitlockite-β-$Ca_3(PO_4)_2$, while the latter peak is similar to the one obtained from tuite-γ-$Ca_3(PO_4)_2$ (Zhai et al. 2014). If we tentatively accept the existence of phosphate in NWA 2975 before the shock event(s), this could be associated with a shock-distorted phosphate grain from NWA 2975 in which precursor tuite held at high residual temperatures and then retrograded into whitlockite (Xie and Chen 2008). In that case, the rock is required to have experienced minimum shock pressures of 14 GPa and temperatures of 1400 °C (Xie et al. 2002).

All plagioclase grains in NWA 2975 have been converted to maskelynite due to shock (see the maskelynite Raman spectrum with two characteristic peaks at 497 and 1007 cm^{-1} in Fig. 6). Previously, for shergottites, the transformation of plagioclase to maskelynite and the presence of other high-pressure phases has been argued to indicate that these samples underwent transient extreme high-pressure events. Earlier studies suggested maskelynite formation required pressures >40 GPa (Stöffler et al. 1991). Stöffler (2000) estimated that the maskelynite in shergottites was produced by shock pressures up to 45 GPa, whereas Fritz et al. (2005) estimated pressures of ~55 GPa., although, more recent studies suggest these pressures overestimate those required for maskelynite transformation (Sharp and DeCarli 2006). Using the method of Fritz et al. (2005), the intensity ratios of the maskelynite 586–507 cm^{-1} Raman bands in NWA 2975 suggest shock pressures in the range of 26–40 GPa. Similarly, we estimated the shock pressures for NWA 2975 to be in the order of 34.4 ± 2.0 GPa on the basis of alkali feldspar cathodoluminescence spectra deconvolution (Kayama et al. 2012). Nevertheless, the peak shock pressure for NWA 2975 could be higher.

Stishovite has been identified as irregularly shaped grains among maskelynite, pigeonite, and Ti-magnetite (Fig. 5D). Synthetic experiments indicate that silica transforms to stishovite, $CaCl_2$-type, α-PbO_2-type (seifertite), and pyrite-type forms with increasing pressure and temperature (Teter et al. 1998; Murakami et al. 2003; Kuwayama et al. 2005). In NWA 2975 BSE images, we observed white and black lamellae intergrowing with each other in amorphous silica (possibly of seifertite) and dense SiO_2 glass (see Figs. 5D, 5D1, and 5D2). Similar textures have been verified from the heavily shocked meteorite Shergotty, with lamellae and dense silica glass occurring together in composite silica grains, and interpreted as evidence for solid-state phase transformation (Sharp et al. 1999; El Goresy et al. 2008, 2013). Further stishovite grains have been verified from Tissint meteorite associated with olivine in melt pockets (Baziotis et al. 2013). It has also been reported intergrowing in some grains with minor stishovite and a new, unnamed, monoclinic dense silica polymorph with α ZrO_2-type structure (El Goresy et al. 2008, 2013). This texture has been ascribed to seifertite formed at pressures above 48 GPa, where stishovite (rutile-type) converts to the $CaCl_2$-structured polymorph (El Goresy et al. 2008, 2013). Bläß (2013) suggested that seifertite back-transformation will produce numerous amorphous lamellae in accordance with our petrographic observations. Additionally, the transition pressure of metastable seifertite could be lower than 30 GPa, within the thermodynamic stability field of stishovite. Recently, Kubo et al. (2015) carried out in situ x-ray diffraction measurements at high pressure and temperature conditions and were able to recover metastable seiferite down to ~11 GPa owing to the different kinetics between seifertite and stable stishovite. Finally, we suggest that the pressure conditions in NWA 2975 were at the range of 11–30 GPa with localized pressure excursions reaching 40 GPa.

Petrogenesis of NWA 2975

The shergottites possess a diverse array of geochemical signatures, with depleted or enriched REE patterns and abundances, different isotopic signatures, and various oxidation states (Herd 2003; Symes et al.

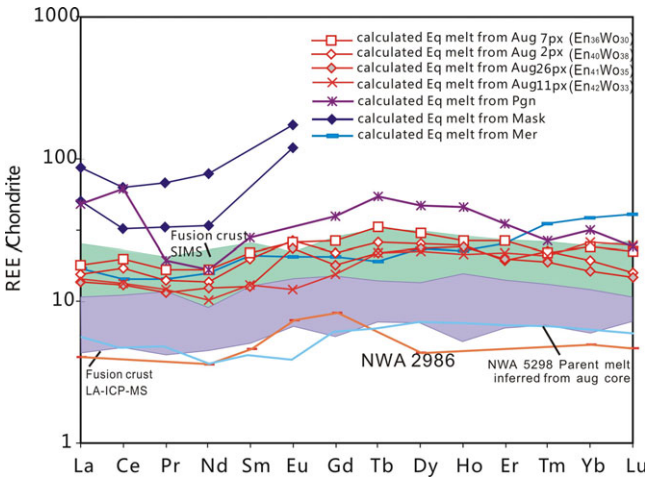

Fig. 10. CI chondrite-normalized REE patterns for calculated melts equilibrated with the cores of augite (Aug), pigeonite (Pgn), plagioclase (Mask), and merrillite (Mer) of NWA 2975. For plagioclase, the highest and lowest REE values are chosen for calculation. Sm, Gd, and HREEs after Gd were not included in the calculation for plagioclase because of large analytical uncertainties. Eu was not included in the calculation for pigeonite because of the large analytical uncertainties. The bulk composition of NWA 2986 was used as an estimate bulk composition of NWA 2975.

2008; Papike *et al*. 2009). Two competing hypotheses have been proposed for the origin of the enrichments observed in the shergottites (1) assimilation of enriched, oxidized crust by mantle-derived magmas (assimilation fractional crystallization, AFC; Jones 1989; Wadhwa 2001; Herd et al. 2002), or (2) mixing of distinct mantle reservoirs during melting (Herd 2003; Borg and Draper 2003).

Using REE partition coefficients appropriate for shergottite magmas (McKay et al. 1986; Lundberg et al. 1990), we calculated the compositions of melts in equilibrium with various primary phases, assuming no REE redistribution after crystallization (Fig. 10). Equilibrium melt compositions calculated from the most Mg-rich augite cores are approximately parallel to REE patterns of NWA 2986 and are within the range of our NWA 2975 fusion crust analyses (Fig. 10). The melts in equilibrium with merrillite have similar calculated REE patterns and abundances to those calculated from pyroxenes.

The REE concentrations of augite cores in NWA 2975 were in equilibrium with the estimated original parent melts, whereas the pigeonites and plagioclases are not. Although open-system processes can cause these types of enrichments in pigeonites and plagioclases, in this case it is likely that both minerals in NWA 2975 have been partially re-equilibrated, most likely during shock. Terrestrial weathering contamination is expected to increase LREE abundances particularly for the pyroxenes which have the lowest La and Ce abundances (Wadhwa et al. 1994; Crozaz and Wadhwa 2001); this effect fits with the elevated La and particularly Ce in the calculated melt in equilibrium with pigeonite. The liquids in equilibrium with plagioclase show REE abundances far higher than those measured in the fusion crust or in liquids in equilibrium with the augites, likely indicating the incorporation of merrillite into the maskelynite during shock. Any assimilation of crustal components during crystallization would be expected to produce elevated pyroxene La and Ce contents due to the low La and Ce content of pyroxene and high expected LREE contents in crustal material (Crozaz and Wadhwa 2001); although our pigeonite signal is disrupted by terrestrial contamination, the correspondence between the liquids calculated to be in equilibrium with augite, those calculated to be in equilibrium with merrillite, and the bulk fusion crust analyses argues against a crustal assimilation signature. Hui et al. (2011) argued that basaltic shergottite NWA 5298 represented closed-system crystallization of an enriched magma, similar to this interpretation. Although neither study can rule out the assimilation of an enriched component prior to the commencement of crystallization, the presence of several meteorites produced by closed-system crystallization of an enriched magma supports the hypothesis of distinct Martian magma sources. Therefore, the composition of and observations made on NWA 2975 are consistent with closed-system chemical behavior during crystallization of an NWA 2975 parental magma produced from a distinct, enriched, Martian magma source.

Oxygen Fugacity from Mineral Equilibrium

Previous studies have shown that Martian magmas have a wide range of oxygen fugacities (fO_2) and correlations among fO_2, La/Yb ratio, and isotopic characteristics (Herd 2003; Symes et al. 2008). We estimated the oxygen fugacity of the NWA 2975 parent magma based on coexisting Fe-Ti oxides (ilmenite-titanomagnetite) using an oxybarometer developed by Ghiorso and Evans (2008). The oxygen fugacity and temperature of NWA 2975 during crystallization of the ilmenite–titanomagnetite pairs were calculated be to NNO -1.86 ± 0.12 (NNO, nickel–nickel oxide buffer) and 870 °C, which puts this meteorite in the oxidized shergottite group (Table 6). This fO_2 is slightly higher than those of Shergotty (NNO -2.25) and Zagami (NNO -2.28), but lower than that of NWA 1068, which is in the range of NNO -0.7 to 0.0 (Herd et al. 2001; Herd 2006). Peslier et al. (2010) argued that fO_2

Table 6. Compositions of Fe-Ti oxides in NWA 2975 used for calculated temperatures and oxygen fugacities.

	SiO_2	TiO_2	Al_2O_3	Cr_2O_3	FeO	MnO	MgO	NiO	T°C (Fe-Ti)	$\log_{10}fO_2$ (NNO)
Ulv	0.20	23.8	1.54	0.34	73.0	0.54	0.30	–	889	−1.71
Ilm	0.14	50.0	0.05	–	48.0	0.63	0.50	–		
Ulv	0.27	23.6	1.79	0.27	73.0	0.51	0.28	–	864	−1.88
Ilm	0.29	50.0	0.06	–	47.7	0.65	0.46	0.02		
Ulv	0.16	24.1	1.87	1.02	71.4	0.46	0.45	0.03	868	−1.98
Ilm	0.21	50.6	0.07	–	47.7	0.57	0.70	–		

Ulv = ulvöspinel; Ilm = ilmenite.

can increase during the shergottite magma differentiation process, producing more oxidized magmas. However, the limited variation in Fe-Ti oxide compositions suggests little change in the oxygen fugacity of NWA 2975 during differentiation. Moreover, the presence of a silica polymorph in contact with Fe-Ti oxides is consistent with the oxygen fugacity of NWA 2975 being around the QFM (fayalite-Magnetite-quartz) buffer (see Fig. 5D). Thus, the oxygen fugacity of NWA 2975 is consistent with a Martian mantle source that is both enriched and oxidized.

Similarity to Other Enriched Shergottites and Crystallization History

As mentioned above, NWA 2975 is an evolved basaltic shergottite similar to Shergotty and Los Angeles; here we compare the observed mineral compositions in these meteorites. The pyroxene cores in NWA 2975 are more ferroan than the pyroxene cores in Shergotty (Hale et al. 1999) and Zagami (McCoy et al. 1992) (Fig 3). Despite these relatively evolved pyroxene compositions in NWA 2975, the plagioclase is not as sodic as in the other meteorites.

Distinct from most other basaltic shergottites, but similar to Los Angeles, the Mg-rich augites in NWA 2975 have slightly higher Mg# than Mg-rich pigeonites (most Mg-rich augite $En_{41.4}Wo_{35.8}$ with Mg# = 0.65, while most Mg-rich pigeonite $En_{50.8}Wo_{13.3}$ with Mg# = 0.59). McCoy and Lofgren (1999) experimentally measured pyroxene-melt Fe-Mg K_D values of ~0.266 for augite and ~0.289 for pigeonite. Applied to the earliest NWA 2975 pyroxenes, these K_D values correlate with parent melt Mg# = 0.33 and 0.29, respectively. This Mg# is comparable to the bulk composition of Dhofar 378 (Mg# = 0.336; Ikeda et al. 2006) and higher than the bulk composition of Los Angeles (Mg# = 0.237; Warren et al. 2000). Given the similarity to the pyroxenes in Los Angeles, it is possible that the K_D calculations are simply under-predicting the Mg# of the coexisting melt under the conditions where NWA 2975 grew.

The crystallization sequence in NWA 2975 can be inferred from its petrography and mineral chemistry. Ti# (molar Ti/[Ti + Cr]) is a useful index for pyroxene crystallization (Joy et al. 2006). Pyroxenes show good correlations between Ti# and Mg# (Fig. 11A) during a typical fractionating basalt trend, as seen in the LaPaz lunar meteorites and Apollo 15 low-Ti basalts (Joy et al. 2006). The cation ratio between Al and Ti in pyroxenes is another useful indicator of concurrent crystallization trends and elemental partitioning in the melt. Plagioclase on the liquidus reduces the amount of Al available for uptake into the pyroxene structure and ilmenite crystallization similarly reduces Ti uptake. Thus, the covariation between Al and Ti, Al/Ti, and Mg# in pyroxenes can additionally support the proposal of a simple crystallization trend. Compositions of pyroxene in NWA 2975 exhibit a good correlation between Al/Ti and Mg#, with decreasing Al when plagioclase cocrystallizes with pyroxene and a fairly constant Al/Ti ratio when both plagioclase and ilmenite crystallize along with pyroxene (Fig. 11B). According to Anand et al. (2006), this correlation indicates elemental partitioning during a simple crystallization sequence. When the Al/Ti value varies from 11:1 to 8:1 or even lower down to 6:1 (Fig. 11B), Mg-rich pyroxene is the main crystallizing phase. Depending on the exact conditions, when the Al/Ti value reaches somewhere between 8:1 to 6:1, plagioclase appears on the liquidus (at about Mg# 0.6; Fig. 11B), consuming Al in the melt, and decreasing the ratio gradually with decreasing Mg# as well. When the ratio reaches around 2, ilmenite begins to crystallize (at about Mg# = 0.4); reducing the Ti content of the melt and keeping the ratio steady until the end of crystallization. Alternatively, Al/Ti values have been proposed as recorders of the pressures that the pyroxene crystallized (Filiberto et al. 2010). A few Mg-rich pyroxenes show high Al/Ti ratio (>10), consistent with crystallization near the base of the Martian crust based on this model. Given the multiple proposals for the cause of the variation in Al/Ti ratios in the literature, we present data in Fig. 11 such that it could be interpreted as either due to pressure decreases or changes in magma composition during

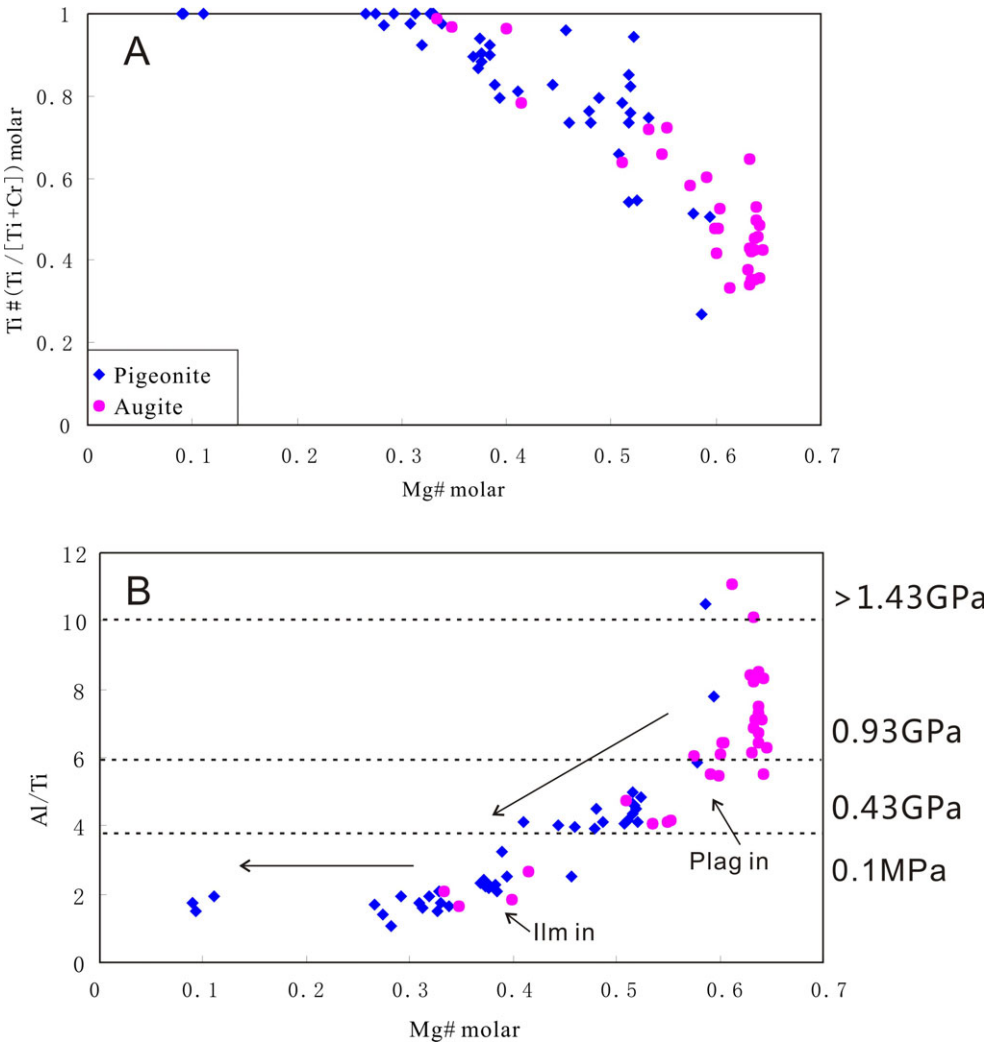

Fig. 11. A) A plot of Ti# versus Mg# for NWA 2975 pyroxenes modified after Joy et al. (2006), showing that pyroxenes in NWA 2975 have a basaltic fractionation trend. B) A plot of atomic Al/Ti ratios versus Mg# for pyroxenes in NWA 2975, indicating the elemental partitioning and crystallization sequence in the melt (Anand et al. 2006). Dashed lines delineate the pressure trends from Nekvasil et al. (2004) and Filiberto et al. (2010). Short arrows indicate plagioclase- and ilmenite-appearance into the crystallizing assemblage, whereas long arrows depict their fractionation path.

crystallization. However, most pyroxenes show low Al/Ti consistent with low-pressure crystallization as a result of upwelling prior to eruption to the Martian surface, and may imply that the Al and Ti variations are driven solely by changes in the composition of the crystallizing magma.

CONCLUSIONS

NWA 2975 is an enriched basaltic shergottite with a medium-grained, subophitic to granular texture. Pyroxenes in NWA 2975 show complex and "patched" compositional zoning that is distinct from that observed in Shergotty and QUE 94201. Mg-rich cores have late-stage Fe-rich rims that often contain exsolution features. Some later crystallized pyroxenes are extremely Fe-rich, suggesting NWA 2975 experienced a prolonged fractionation history. The major element composition of NWA 2975 fusion crust is comparable to those of other enriched basaltic shergottites.

The CI chondrite normalized REE patterns of NWA 2975 fusion crust are flat and parallel to those of "enriched" basaltic shergottites. REE contents of augite cores in NWA 2975 were in equilibrium with the original parent melts, whereas the pigeonites and maskelynite were re-equilibrated during shock.

The oxidation state is NNO −1.86, close to the QFM buffer. Therefore, NWA 2975 represents a sample

of the oxidized and enriched shergottite group with no evidence of crustal contamination, arguing in favor of the existence of two distinct Martian mantle reservoirs: the reduced, LREE-depleted reservoir and oxidized, LREE-enriched reservoir. We observed stishovite, possibly of seifertite and dense SiO_2 glass in this sample. Based on these observations, our best estimate of the shock pressure conditions experienced by NWA 2975 is in the range of 11–30 GPa, with localized pressure higher up to 40 Gpa.

Acknowledgments—This manuscript greatly benefits from reviews by J. Bridges and an anonymous reviewer, as well as reviewers of previous versions. The associate editor Akira Yamaguchi and main editor Timothy Jull are also gratefully acknowledged. This study was supported by the Natural Science Foundation of China (no. 41303050), the Fundamental Research Funds for the Central Universities, China University of Geosciences (Wuhan), and the Advantages of the Doctoral Degree Field Project (20130145130001). Dr. Ke Zuokai from School of Geosciences and Info-Physics, Central South University, China provided the sample used in this study. We also thank Mr. Tan Jianyun for his help in making the thin section, Dr. Zheng Jianping for assistance with Raman spectrum analysis, and Dr. Zong Keqing for LA-ICP-MS analysis.

Editorial Handling—Dr. Akira Yamaguchi

REFERENCES

Agee C. B., Wilson N. V., McCubbin F. M., Ziegler K., Polyak V. J., Sharp Z. D., Asmerom Y., Nunn M. H., Shaheen R., Thiemens M. H., Steele A., Fogel M. L., Bowden R., Glamoclija M., Zhang Z., and Elardo S. M. 2013. Unique meteorite from early Amazonian Mars: Water-rich basaltic breccia Northwest Africa 7034. *Science* 339:780–785.

Anand M., Taylor L. A., Floss C., Neal C., Terada K., and Tanikawa S. 2006. Petrology and geochemistry of LaPaz Icefield 02205: A new unique low-Ti mare-basalt meteorite. *Geochimica et Cosmochimica Acta* 70:246–264.

Aramovich C. J., Herd C. D. K., and Papike J. J. 2002. Symplectites derived from metastable phases in Martian basaltic meteorites. *American Mineralogist* 87:1351–1359.

Balta J. B., Sanborn M. E., Udry A., Wadhwa M., and McSween H. Y. 2015. Petrology and trace element geochemistry of Tissint, the newest shergottite fall. *Meteoritics & Planetary Science* 50:63–85.

Baziotis I. P., Liu Y., DeCarli P. S., Melosh H. J., McSween H. Y., Bodnar R. J., and Taylor L. A. 2013. The Tissint Martian meteorite as evidence for the largest impact excavation. *Nature Communications* 4:1404.

Beck P., Gillet P., Gautron L., Daniel I., and El Goresy A. 2004. A new natural high-pressure (Na, Ca)-hexaluminosilicate [$(Ca_xNa_{1-x})Al_{3+x}Si_{3-x}O11$] in shocked Martian meteorites. *Earth and Planetary Science Letters* 219:1–12.

Beck P., Gillet P., El Goresy A., and Mostefaoui S. 2005. Timescales of shock processes in chondritic and Martian meteorites. *Nature* 435:1071–1074.

Bläß U. W. 2013. Shock-induced formation mechanism of seifertite in shergottites. *Physics and Chemistry of Minerals* 40:425–437.

Borg L. E. and Draper D. S. 2003. A petrogenetic model for the origin and compositional variation of the Martian basaltic meteorites. *Meteoritics & Planetary Science* 38:1713–1731.

Bouvier A., Vervoort J. D., and Patchett P. J. 2005. The age of SNC meteorites and the antiquity of the Martian surface. *Earth and Planetary Science Letters* 240:221–233.

Brandon A. D., Walker R. J., Morgan J. W., and Goles G. G. 2000. Re-Os isotopic evidence for early differentiation of the Martian mantle. *Geochimica et Cosmochimica Acta* 64:4083–4095.

Bridges J. C. and Warren P. H. 2006. The SNC meteorites: Basaltic igneous processes on Mars. *Journal of the Geological Society* 163:229–251.

Chen M., Topeka B., Xie X., and EI Goresy A. 1995. A new high-pressure polymorph of chlorapatite in the shocked sixiangkou (L6) chondrite. Proceedings, 36th Lunar and Planetary Science Conference. pp. 237–238.

Crozaz G. and Wadhwa M. 2001. The terrestrial alteration of Saharan shergottites Dar al Gani 476 and 489: A case study of weathering in a hot desert environment. *Geochimica et Cosmochimica Acta* 65:971–977.

Day J. M. D., Taylor L. A., Floss C., Patchen A. D., Schnare D. W., and Pearson D. G. 2006. Comparative petrology, geochemistry, and petrogenesis of evolved, low-Ti lunar mare basalt meteorites from the LaPaz Icefield, Antarctica. *Geochimica et Cosmochimica Acta* 70:1581–1600.

Debaille V., Yin Q. Z., Brandon A. D., and Jacobsen B. 2008. Martian mantle mineralogy investigated by the ^{176}Lu-^{176}Hf and ^{147}Sm-^{143}Nd systematics of shergottites. *Earth and Planetary Science Letters* 269:186–199.

Downs R. T. 2006. The RRUFF project: An integrated study of the chemistry, crystallography, Raman and infrared spectroscopy of minerals. Program and Abstracts of the 19th General Meeting of the International Mineralogical Association in Kobe, Japan. O03-13.

El Goresy A., Dubrovinsky L., Sharp T. G., and Chen M. 2004. Stishovite and post-stishovite polymorphs of silica in the shergotty meteorite: Their nature, petrographic settings versus theoretical predictions and relevance to Earth's mantle. *Journal of Physics and Chemistry of Solids* 65:1597–1608.

El Goresy A., Dera P., Sharp T. G., Prewitt C. T., Chen M., Dubrovinsky L., Topeka B., Boctor N. Z., and Hemley R. J. 2008. Seifertite, a dense orthorhombic polymorph of silica from the Martian meteorites Shergotty and Zagami. *European Journal of Mineralogy* 20:523–528.

El Goresy A., Gillet P., Miyahara M., Ohtani E., Ozawa S., Beck P., and Montagnac G. 2013. Shock-induced deformation of Shergottites: Shock-pressures and perturbations of magmatic ages on Mars. *Geochimica et Cosmochimica Acta* 101:233–262.

Filiberto J., Musselwhite D. S., Gross J., Burgess K., Le L., and Treiman A. H. 2010. Experimental petrology, crystallization history, and parental magma characteristics of olivine-phyric shergottite NWA 1068: Implications for

the petrogenesis of "enriched" olivine-phyric shergottites. *Meteoritics & Planetary Science* 45:1258–1270.

Fritz J. R., Artemieva N., and Greshake A. 2005. Ejection of Martian meteorites. *Meteoritics & Planetary Science* 40:1393–1411.

Ghiorso M. S. and Evans B. W. 2008. Thermodynamics of rhombohedral oxide solid solutions and a revision of the Fe-Ti two-oxide geothermometer and oxygen-barometer. *American Journal of Science* 308:957–1039.

Gnos E., Hofmann B., Franchi I. A., Al-Kathiri A., Hauser M., and Moser L. 2002. Sayh al Uhaymir 094: A new Martian meteorite from the Oman desert. *Meteoritics & Planetary Science* 37:835–854.

Goodrich C. A. 2002. Olivine-phyric Martian basalts: A new type of shergottite. *Meteoritics & Planetary Science* 37: B31–B34.

Goodrich C. A. 2003. Petrogenesis of olivine-phyric shergottites Sayh Al Uhaymir 005 and elephant moraine A79001 lithology A. *Geochimica et Cosmochimica Acta* 67:3735–3772.

Greenwood J. P., Blake R. E., and Coath C. D. 2003. Ion microprobe measurements of $^{18}O/^{16}O$ ratios of phosphate minerals in the Martian meteorites ALH84001 and Los Angeles. *Geochimica et Cosmochimica Acta* 67:2289–2298.

Hale V. P. S., McSween H. Y. Jr., and McKay G. A. 1999. Re-evaluation of intercumulus liquid composition and oxidation state for the Shergotty meteorite. *Geochimica et Cosmochimica Acta* 63:1459–1470.

He Q., Hsu W., Xiao L., and Guan Y. 2011. Petrography and geochemistry of the Shergottite Northwest Africa 2975 (abstract #1646). 42nd Lunar and Planetary Science Conference. CD-ROM.

Hemley R. J., Mao H. K., and Chao E. C. T. 1986. Raman spectrum of natural and synthetic stishovite. *Physics and Chemistry of Minerals* 13:285–290.

Herd C. D. 2003. The oxygen fugacity of olivine-phyric Martian basalts and the components within the mantle and crust of Mars. *Meteoritics & Planetary Science* 38:1793–1805.

Herd C. D. 2006. Insights into the redox history of the NWA 1068/1110 Martian basalt from mineral equilibria and vanadium oxybarometry. *American Mineralogist* 91:1616–1627.

Herd C. D., Papike J. J., and Brearley A. J. 2001. Oxygen fugacity of Martian basalts from electron microprobe oxygen and TEM-EELS analyses of Fe-Ti oxides. *American Mineralogist* 86:1015–1024.

Herd C. D., Borg L. E., Jones J. H., and Papike J. J. 2002. Oxygen fugacity and geochemical variations in the Martian basalts: Implications for Martian basalt petrogenesis and the oxidation state of the upper mantle of Mars. *Geochimica et Cosmochimica Acta* 66:2025–2036.

Herd C. D., Simonetti A., and Peterson N. D. 2007. In situ U-Pb geochronology of Martian baddeleyite by laser ablation MC-ICP-MS (abstract #1664). 38th Lunar and Planetary Science Conference. CD-ROM.

Hsu W., Guan Y., Wang H., Leshin L. A., Wang R., Zhang W., Chen X., Zhang F., and Lin C. 2004. The lherzolitic shergottite Grove Mountains 99027: Rare earth element geochemistry. *Meteoritics & Planetary Science* 39:701–709.

Hu Z., Gao S., Liu Y., Hu S., Chen H., and Yuan H. 2008. Signal enhancement in laser ablation ICP-MS by addition of nitrogen in the central channel gas. *Journal of Analytical Atomic Spectrometry* 23:1093–1101.

Hui H., Peslier A. H., Lapen T. J., Shafer J. T., Brandon A. D., and Irving A. J. 2011. Petrogenesis of basaltic shergottite Northwest Africa 5298: Closed-system crystallization of an oxidized mafic melt. *Meteoritics & Planetary Science* 46:1313–1328.

Ikeda Y., Kimura M., Takeda H., and Suzuki A. 2006. Peteology of a new basaltic shergottite: Dhofar 378. *Antarctic Meteorite Research* 19:20–44.

Irving A. J., Herd C. D. K., Kuehner S. M., Gregory D. A., and Aaronson A. A. 2004. Petrology and redox state of basaltic shergottite NWA 3171. *Geochimica et Cosmochimica Acta* 39:A49.

Jambon A., Barrat J. A., Sautter V., Gillet P., Göpel C., Javoy M., Joron J. L., and Lesourd M. 2002. The basaltic shergottite Northwest Africa 856: Petrology and chemistry. *Meteoritics & Planetary Science* 37:1147–1164.

Jones J. H. 1989. Isotopic relationships among the shergottites, the nakhlites, and Chassigny. Proceedings, 19th Lunar and Planetary Science Conference. pp. 465–474.

Joy K. H., Crawford I. A., Downes H., Russell S. S., and Kearsley A. T. 2006. A petrological, mineralogical, and chemical analysis of the lunar mare basalt meteorite LaPaz Icefield 02205, 02224, and 02226. *Meteoritics & Planetary Science* 41:1003–1025.

Kayama M., Nishido H., Sekine T., Nakazato T., Gucsik A., and Ninagawa K. 2012. Shock barometer using cathodoluminescence of alkali feldspar. *Journal of Geophysical Research: Planets* 117:E09004:1–13.

Kubo T., Kato T., Higo Y., and Funakoshi K. I. 2015. Curious kinetic behavior in silica polymorphs solves seifertite puzzle in shocked meteorite. *Science Advances* 1.4:e1500075.

Kuwayama Y., Hirose K., Sata N., and Ohishi Y. 2005. The pyrite-type high-pressure form of silica. *Science* 309:923–925.

Langenhorst F. and Poirier J. P. 2000. Anatomy of black veins in Zagami: Clues to the formation of high-pressure phases. *Earth and Planetary Science Letters* 184:37–55.

Lapen T. J., Righter M., Brandon A. D., Debaille V., Beard B. L., Shafer J. T., and Peslier A. H. 2010. A younger age for ALH 84001 and its geochemical link to shergottite sources in Mars. *Science* 328:347–351.

Lindsay F. N., Osmond J., Delaney J. S., Herzog G. F., Turrin B., Park J., and Swisher C. C. 2013. Ar/Ar systematics of Martian meteorite NWA 2975 (abstract #2911). 44th Lunar and Planetary Science Conference. CD-ROM.

Lindsley D. H. and Burnham C. W. 1970. Pyroxferroite: Stability and X-ray crystallography of synthetic $Ca_{0.15}Fe_{0.85}SiO_3$ pyroxenoid. *Science* 168:364–367.

Lindsley D. H., Papike J. J., and Bence A. E. 1972. Pyroxferroite: Breakdown at low pressure and high temperature (abstract). 3rd Lunar Science Conference. p. 483.

Liu Y. S., Hu Z. C., Gao S., Günther D., Xu J., Gao C. G., and Chen H. H. 2008. In situ analysis of major and trace elements of anhydrous minerals by LA-ICP-MS without applying an internal standard. *Chemical Geology* 257:34–43.

Liu Y. S., Hu Z. C., Zong K. Q., Gao C. G., Gao S., Xu J., and Chen H. H. 2010. Reappraisement and refinement of zircon U-Pb isotope and trace element analyses by LA-ICP-MS. *Chinese Science Bulletin* 55:1535–1546.

Lundberg L. L., Crozaz G., McKay G., and Zinner E. 1988. Rare earth element carriers in the Shergotty meteorite and implications for its chronology. *Geochimica et Cosmochimica Acta* 52:2147–2163.

Lundberg L. L., Crozaz G., and McSween H. Y. 1990. Rare earth elements in minerals of the ALHA77005 shergottite and implications for its parent magma and crystallization history. *Geochimica et Cosmochimica Acta* 54:2535–2547.

McCoy T. J. and Lofgren G. E. 1999. Crystallization of the Zagami shergottite: An experimental study. *Earth and Planetary Science Letters* 173:397–411.

McCoy T. J., Taylor G. J., and Keil K. 1992. Zagami: Product of a two-stage magmatic history. *Geochimica et Cosmochimica Acta* 56:3571–3582.

McCoy T. J., Wadhwa M., and Keil K. 1999. New lithologies in the Zagami meteorite: Evidence for fractional crystallization of a single magma unit on Mars. *Geochimica et Cosmochimica Acta* 63:1249–1262.

McCubbin F. M., Hauri E. H., Elardo S. M., Vander Kaaden K. E., Wang J., and Shearer C. K. 2012. Hydrous melting of the martian mantle produced both depleted and enriched shergottites. *Geology* 40:683–686.

McKay G., Wagstaff J., and Yang S. R. 1986. Clinopyroxene REE distribution coefficients for shergottites: The REE content of the Shergotty melt. *Geochimica et Cosmochimica Acta* 50:927–937.

McSween H. Y. Jr., Eisenhour D. D., Taylor L. A., Wadhwa M., and Crozaz G. 1996. QUE94201 shergottite: Crystallization of a Martian basaltic magma. *Geochimica et Cosmochimica Acta* 60:4563–4569.

Meyer C. 2012. Martian Meteorite Compendium. http://curator.jsc.nasa.gov/antmet/mmc/. Accessed 2012.

Mikouchi T., Miyamoto M., and McKay G. A. 1999. The role of undercooling in producing igneous zoning trends in pyroxenes and maskelynites among basaltic Martian meteorites. *Earth and Planetary Science Letters* 173:235–256.

Misawa K. and Yamaguchi A. 2007. U-Pb ages of NWA 856 baddeleyite. *Meteoritics & Planetary Science* 42:A108.

Moser D. E., Chamberlain K. R., Tait K. T., Schmitt A. K., Darling J. R., Barker I. R., and Hyde B. C. 2013. Solving the Martian meteorite age conundrum using micro-baddeleyite and launch-generated zircon. *Nature* 499:454–457.

Murakami M., Hirose K., Ono S., and Ohishi Y. 2003. Stability of $CaCl_2$-type and α-PbO_2 at high pressure and temperature determined by in-situ X-ray measurements. *Geophysical Research Letters* 30:1207.

Nekvasil H., Dondolini A., Horn J., Filiberto J., Long H., and Lindsley D. H. 2004. The origin and evolution of silica saturated alkalic suites: An experimental study. *Journal of Petrology* 45:693–721.

Niihara T. 2011. Uranium-lead age of baddeleyite in shergottite Roberts Massif 04261: Implications for magmatic activity on Mars. *Journal of Geophysical Research: Planets* 116:E12.

Nyquist L. E., Bogard D. D., Shih C. Y., Greshake A., Stöffler D., and Eugster O. 2001. Ages and geologic histories of Martian meteorites. *Space Science Reviews* 96:105–164.

Papike J. J. 1998. Comparative planetary mineralogy: Chemistry of melt-derived pyroxene, feldspar, and olivine. In *Planetary materials*, edited by Papike J. J. Reviews in Mineralogy, vol. 36. Washington, D.C.: Mineralogical Society of America. 7-01–07-10.

Papike J. J., Karner J. M., and Shearer C. K. 2003. Determination of planetary basalt parentage: A simple technique using the electron microprobe. *American Mineralogist* 88:469–472.

Papike J. J., Karner J. M., Shearer C. K., and Burger P. V. 2009. Silicate mineralogy of Martian meteorites. *Geochimica et Cosmochimica Acta* 73:7443–7485.

Peslier A. H., Hnatyshin D., Herd C. D. K., Walton E. L., Brandon A. D., Lapen T. J., and Shafer J. T. 2010. Crystallization, melt inclusion, and redox history of a Martian meteorite: Olivine-phyric shergottite Larkman Nunatak 06319. *Geochimica et Cosmochimica Acta* 74:4543–4576.

Rubin A. E., Warren P. H., Greenwood J. P., Verish R. S., Leshin L. A., Hervig R. L., Clayton R. N., and Mayeda T. K. 2000. Los Angeles: The most differentiated basaltic Martian meteorite. *Geology* 28:1011–1014.

Sanborn M. E. and Wadhwa M. 2010. Trace element geochemistry of the basaltic shergottite Northwest Africa 2975. *Meteoritics & Planetary Science Supplement* 73:5294.

Sharp T. G. and DeCarli P. S. 2006. Shock effect in meteorites. In *Meteorites and the early solar system II*, edited by Lauretta D. S. and McSween H. Y. Jr. Tucson, Arizona: University of Arizona Press. pp. 653–677.

Sharp T. G., El Goresy A., Topeka B., and Chen M. 1999. A post-stishovite SiO_2 polymorph in the meteorite Shergotty: Implications for impact events. *Science* 284:1511–1513.

Steele I. M. and Smith J. V. 1982. Petrography and mineralogy of two basalts and olivine-pyroxene-spinel fragments in achondrite EETA79001. *Journal of Geophysical Research* 87:A375–A384.

Stöffler D. 2000. Maskelynite confirmed as diaplectic glass: Indication for peak shock pressures below 45 GPa in all Martian meteorites (abstract #1170). 31st Lunar and Planetary Institute Science Conference. CD-ROM.

Stöffler D., Ostertag R., Jammes C., Pfannschmidt G., Gupta P. R., Simon S. B., Papike J. J., and Beauchamp R. H. 1986. Shock metamorphism and petrography of the Shergotty achondrite. *Geochimica et Cosmochimica Acta* 50:889–903.

Stöffler D., Keil K., and Scott E. R. D. 1991. Shock metamorphism of ordinary chondrites. *Geochimica et Cosmochimica Acta* 55:3845–3867.

Stolper E. and McSween H. Y. 1979. Petrology and origin of the shergottite meteorites. *Geochimica et Cosmochimica Acta* 43:1475–1498.

Symes S. J., Borg L. E., Shearer C. K., and Irving A. J. 2008. The age of the Martian meteorite Northwest Africa 1195 and the differentiation history of the shergottites. *Geochimica et Cosmochimica Acta* 72:1696–1710.

Tait K. T., Irving A. J., Nicklin R. I., Day J. M. D., Andreasen R., Kuehner S. M., Ziegler K., and Lapen T. J. 2015. Petrologic and isotopic characterization of enriched mafic shergottite Northwest Africa 8679 (abstract #2709). 46th Lunar and Planetary Science Conference. CD-ROM.

Teter D. M., Hemley R. J., Kresse G., and Hafner J. 1998. High pressure polymorphism in silica. *Physical Review Letters* 80:2145.

Thaisen K. G. and Taylor L. A. 2009. Meteorite fusion crust variability. *Meteoritics & Planetary Science* 44:871–878.

Treiman A. H. 2005. The nakhlite meteorites: Augite-rich igneous rocks from Mars. *Chemie der Erde-Geochemistry* 65:203–270.

Wadhwa M. 2001. Redox state of Mars' upper mantle and crust from Eu anomalies in shergottite pyroxenes. *Science* 291:1527–1530.

Wadhwa M., McSween H. Y. Jr, and Crozaz G. 1994. Petrogenesis of shergottite meteorites inferred from minor and trace element microdistributions. *Geochimica et Cosmochimica Acta* 58:4213–4229.

Wang A., Jolliff B., Viskupic K. M., and Haskin L. A. 1997. Raman spectroscopic characterization of different types of pyroxene (abstract #1384). 28th Lunar and Planetary Science Conference. CD-ROM.

Wang A., Kuebler K. E., Jolliff B. L., and Haskin L. A. 2004a. Raman spectroscopy of Fe-Ti-Cr-oxides, case study: Martian meteorite EETA79001. *American Mineralogist* 89:665–680.

Wang A., Kuebler K., Jolliff B., and Haskin L. A. 2004b. Mineralogy of a Martian meteorite as determined by Raman spectroscopy. *Journal of Raman Spectroscopy* 35:504–514.

Wang Y., Hsu W., Guan Y., Li X., Li Q., Liu Y., and Tang G. 2012. Petrogenesis of the Northwest Africa 4734 basaltic lunar meteorite. *Geochimica et Cosmochimica Acta* 92:329–344.

Warren P. H., Greenwood J. P., Richardson J. W., Rubin A. E., and Verish R. S. 2000. Geochemistry of Los Angeles, a ferroan, La-and Th-rich basalt from Mars (abstract #2001). 31st Lunar and Planetary Science Conference. CD-ROM.

Warren P. H., Greenwood J. P., and Rubin A. E. 2004. Los Angeles: A tale of two stones. *Meteoritics & Planetary Science* 39:137–156.

Wittke J. H., Bunch T. E., Irving A. J., Farmer M., and Strope J. 2006. Northwest Africa 2975: An evolved basaltic shergottite with vesicular glass pockets and trapped melt inclusions (abstract #1368). 37th Lunar and Planetary Science Conference. CD-ROM.

Xie X. and Chen M. 2008. Formation conditions of tuite. *Geochemica* 37:297–303.

Xie X., Minitti M. E., Chen M., Mao H. K., Wang D., Shu J., and Fei Y. 2002. Natural high pressure polymorph of merrillite in the shock veins of the Suizhou meteorite. *Geochimica et Cosmochimica Acta* 66:2439–2444.

Zhai S., Akaogi M., Kojitani H., Xue W., and Ito E. 2014. Thermodynamic investigation on β- and γ-$Ca_3(PO_4)_2$ and the phase equilibria. *Physics of the Earth and Planetary Interiors* 228:144–149.

Zhou Q., Herd C. D., Yin Q., Li X., Wu F., Li Q., Liu Y., Tang G., and McCoy T. J. 2013. Geochronology of the Martian meteorite Zagami revealed by U-Pb ion probe dating of accessory minerals. *Earth and Planetary Science Letters* 374:156–163.

SUPPORTING INFORMATION

Additional supporting information may be found in the online version of this article:

Table S1. EMP (in wt%) analyses of fusion crust.

Table S2. Trace element compositions (in ppm) of minerals and fusion crust by SIMS for NWA 2975.

Table S3. LA-ICP-MS analyses result of fusion crust and melt pocket (or vein).